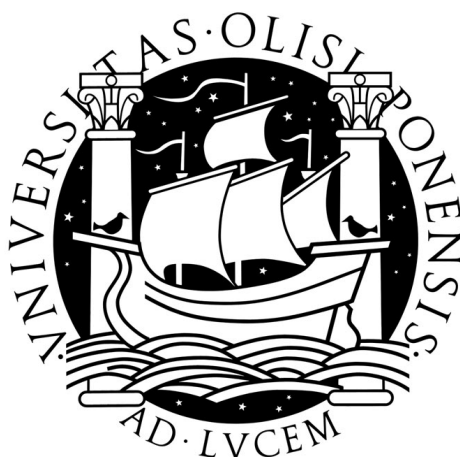


Universidade de Lisboa
Faculdade de Ciências
Departamento de Física



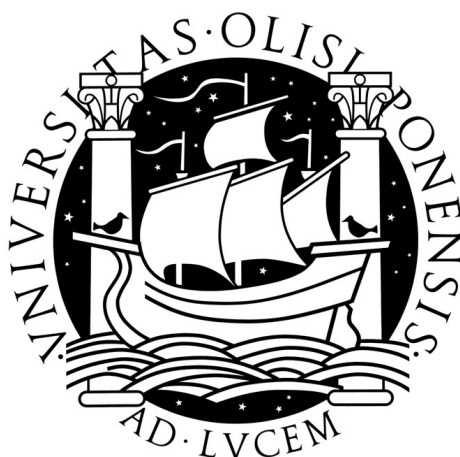
Implementation and Evaluation of Different Scaling Methods in Single Scatter Simulation for the Siemens BrainPET scanner

João André de Matos Monteiro

DISSERTAÇÃO

MESTRADO INTEGRADO EM ENGENHARIA BIOMÉDICA E BIOFÍSICA
PERFIL EM RADIAÇÕES EM DIAGNÓSTICO E TERAPIA

Universidade de Lisboa
Faculdade de Ciências
Departamento de Física



Implementation and Evaluation of Different Scaling Methods in Single Scatter Simulation for the Siemens BrainPET scanner

João André de Matos Monteiro

DISSERTAÇÃO

MESTRADO INTEGRADO EM ENGENHARIA BIOMÉDICA E BIOFÍSICA
PERFIL EM RADIAÇÕES EM DIAGNÓSTICO E TERAPIA

Orientador Externo: Doutor Jürgen Scheins
Orientador Interno: Professor Doutor Pedro Almeida

2012

This thesis is dedicated to my parents and my sister.

Acknowledgements

This thesis had the help of many people at the Institute of Neuroscience and Medicine (INM-4) of the Forschungszentrum Jülich, at the Faculty of Sciences of the University of Lisbon and at the Institute of Biophysics and Biomedical Engineering, to whom I would like to thank.

This project would not have been possible without the help of my external supervisor, Doctor Jürgen Scheins, who guided me during my work, corrected my thesis and explained me how to work with the software tools developed at the Forschungszentrum Jülich. I would like to thank him for all the time that he spent in these tasks.

The help of my internal supervisor, Professor Pedro Almeida, was also essential. I would like to thank him for supporting me into doing my thesis in PET, for providing the contact with the PET group at the Forschungszentrum Jülich and for correcting my thesis.

I would also like to thank Professor Hans Herzog for receiving me in his group and for helping me and my colleagues with all the bureaucratic issues that we had.

Before my colleagues and I came to Jülich, we had some difficulties finding accommodation. I have to thank Doctor Elena Rota Kops for helping us in this difficult task.

During my first weeks at the Forschungszentrum Jülich, I had to learn how PET works on a more advanced level and how to use the different software tools. A lot of the questions that I had were answered by Liliana Caldeira, who has my gratitude for her patience.

The real data in this report was acquired by Christoph Weirich, to whom I thank for letting me use them in my own tests. I would also like to thank Lutz Tellmann for providing me with the information and attenuation map of the phantom used in the acquisition of real data.

The funding that I received from the Erasmus Programme was essential for this project. I would like to thank the University of Lisbon for the funding and Professor Guiomar Evans for helping me with the bureaucratic issues related to it.

Finally, I would like to thank my colleagues André Ribero, Nuno André da Silva, Philipp Lohmann and Martin Weber for all the interesting conversations that we had in the office and for all the good times that we spent outside of it. Also, to everyone else that I might have forgotten.

Resumo

A Tomografia por Emissão de Positrões (PET, do Inglês *Positron Emission Tomography*) trata-se de uma técnica de medicina nuclear a qual é bastante importante no diagnóstico de diversas patologias. Utiliza radiofármacos com um tempo de meia-vida curto, de modo a obter uma imagem de emissão.

A taxa de absorção do radiofármaco varia de acordo com o tipo de tecido. Este fenómeno é especialmente importante no diagnóstico de cancro, uma vez que o metabolismo das células tumorais é superior, o que resulta numa maior taxa de absorção do radiofármaco por parte destas células, comparativamente com as células saudáveis. Este fenómeno permite a aquisição de uma imagem funcional.

Tal como o nome indica, a PET baseia-se na emissão de positrões pelos radionuclídeos. Cada positrão irá aniquilar-se com um electrão, produzindo dois fótons γ de 511 keV, os quais são detectados pelo sistema de PET e utilizados para reconstruir uma imagem da distribuição do radiofármaco. A qualidade da imagem é influenciada por vários factores, sendo a dispersão de Compton um dos mais importantes. Este fenómeno provoca uma deflexão na trajectória original dos fótons, resultando na deterioração do contraste da imagem.

Actualmente, é possível estimar a quantidade de eventos detectados pelo sistema de PET que sofreram dispersão de Compton e corrigir os dados adquiridos. Vários métodos foram propostos ao longo dos anos para corrigir os dados, sendo bastante utilizados os algoritmos baseados em modelos físicos. Dentro destes, um dos mais importantes é o *Single Scatter Simulation* (SSS), o qual permite estimar a distribuição de eventos dispersos por interações de Compton e representar os resultados em sinogramas de dispersão. Contudo, estes sinogramas não se encontram escalados, sendo este passo executado separadamente. Os métodos de escalamento utilizam as contagens detectadas fora do objecto que foi medido (conhecidas como *scatter tails*) como referência. Um dos problemas relacionados com o escalamento advém do facto destas regiões possuírem contagens muito baixas, o que as torna susceptíveis a ruído de Poisson, dificultando a estimação do factor de escalamento correcto.

Este projecto fez uso de dados adquiridos e simulados para o *scanner* BrainPET da Siemens instalado no Forschungszentrum Jülich. Actualmente, o escalamento dos sinogramas de dispersão é feito utilizando os pacotes de *software* disponibilizados pelo fabricante, os quais demonstraram resultados razoáveis podendo, no entanto, ser melhorados.

O objectivo principal deste trabalho consiste na implementação e avaliação

de diversos métodos de escalamento dos sinogramas de dispersão, tanto novos como previamente existentes, tendo em vista melhorar o passo de escalamento do SSS. Isto permitirá uma melhor correcção do efeito da dispersão de Compton nos dados, melhorando a qualidade das imagens de PET.

Foram também testados em dados simulados, diversos factores que podem introduzir erros no escalamento dos sinogramas de dispersão, de modo a documentar a sua influência na imagem reconstruída. Os factores testados foram o escalamento incorrecto dos sinogramas de dispersão e o escalamento incorrecto dos sinogramas de eventos aleatórios. Foi também testada a utilização de uma imagem corrigida para atenuação e eventos aleatórios para a estimação dos sinogramas de dispersão em vez de um fantoma gerado matematicamente.

No capítulo 2 são introduzidos os conceitos físicos básicos necessários à compreensão do funcionamento dos sistemas de PET. São também expostos os diferentes procedimentos utilizados para adquirir, organizar e corrigir dados, bem como alguns algoritmos de reconstrução.

O capítulo 3 foca-se na descrição do *scanner* BrainPET, nos métodos que foram implementados para escalar os sinogramas de dispersão e nos processos necessários para adquirir os dados utilizados, tanto reais como simulados.

Os dados simulados foram adquiridos gerando três conjuntos de sinogramas (sinogramas de eventos verdadeiros não-dispersos, sinogramas de eventos aleatórios e sinogramas de dispersão), somando-os e introduzindo ruído de Poisson. Estes dados foram divididos em cinco grupos, consoante o número de eventos verdadeiros não-dispersados: 1×10^6 , 1×10^7 , 1×10^8 , 1×10^9 e 1×10^{10} . Esta divisão permitiu estudar o comportamento de cada método de escalamento a diferentes níveis estatísticos.

Os dados reais foram adquiridos utilizando um fantoma cilíndrico com uma concentração uniforme de ^{18}F .

Foram implementados três métodos de escalamento. O primeiro, denominado de *Standard*, é actualmente utilizado no Forschungszentrum Jülich. O segundo, é bastante semelhante ao *Standard*, mas utiliza os dados sem aplicar pré-correcção, designando-se *Non Pre-Corrected Data* (NPCD) *scaling method*. O terceiro, aborda o escalamento de uma maneira diferente dos outros dois, denomina-se *Maximum Likelihood* (ML) *scaling method* e tem em conta o ruído de Poisson na estimação do factor de escalamento.

Os métodos foram testados quer para um único plano no centro do segmento 0, quer para vários planos, comparando a utilização de um filtro *boxcar* ou a integração de planos adjacentes (PI, do Inglês *Plane Integration*).

Os resultados obtidos encontram-se descritos no capítulo 4.

Os novos métodos de escalamento (NPCD e ML) foram comparados com o método utilizado actualmente para correcção de dispersão de Compton no *scanner* BrainPET (*Standard*). Estes demonstraram que, para um único plano, os resultados foram melhores que o método utilizado actualmente. O NPCD mostrou uma melhoria de cerca de 4% e o ML uma melhoria de cerca de 13% a todos os níveis estatísticos.

Caso sejam utilizados mais planos para estimar os factores de escalamento, os

resultados mostraram que para o método *Standard* e para o método NPCD não parece existir nenhuma vantagem em usar PI em vez do filtro *boxcar* actualmente utilizado. Contudo, aquando da utilização do método ML, a PI conferiu uma melhoria de cerca de 1% em relação ao filtro *boxcar* a todos os níveis estatísticos.

Todos os métodos de escalamento demonstraram um comportamento semelhante à introdução de erros nos dados. A influência de cada fonte de erros foi estudada de modo a verificar o seu efeito na imagem reconstruída. Os resultados deverão demonstrar-se úteis como referência futura, caso seja necessário identificar uma fonte de erro nos dados.

Apesar dos resultados positivos adquiridos no escalamento, os procedimentos de reconstrução não foram tão bem sucedidos. Estes demonstraram ser tendenciosos caso a estimação dos sinogramas de dispersão não seja feita com o fantoma gerado matematicamente. Este problema pode ser resolvido em dados simulados caso a estimação dos sinogramas de dispersão e reconstrução sejam efectuados várias vezes, mesmo para fracções de dispersão de Compton superiores ou em objectos mais complexos do que um cilindro uniforme.

Os dados reais adquiridos com o fantoma cilíndrico foram reconstruídos utilizando o procedimento de rotina, demonstrando os mesmos problemas. Contudo, neste caso a repetição da estimação dos sinogramas de dispersão e reconstrução não resolveram o problema. Ao contrário do que foi observado em dados simulados, a estimação dos sinogramas de dispersão com uma imagem de um cilindro uniforme não resultou numa imagem não tendenciosa. Sendo que nestes dados não foi possível reconstruir uma imagem não tendenciosa, nem pela utilização do fantoma para estimar os sinogramas de dispersão nem pela repetição da estimação e reconstrução. Isto pode ser devido ao facto do SSS não considerar casos de dispersão múltipla, em que um ou ambos os fotões γ são dispersados mais do que uma vez por interacções de Compton.

Os resultados mostrados nas secções 4.1.1 e 4.1.2 sugerem que a utilização do método ML com PI pode ser uma boa alternativa ao método actualmente utilizado. Contudo, devem ser realizados mais estudos, tanto com dados simulados como com dados reais.

Actualmente existe um *toolkit* desenvolvido no Forschungszentrum Jülich denominado *PET REconstruction Software TOolkit* (PRESTO). Caso o método ML continue a mostrar melhores resultados que o método utilizado actualmente, este poderá ser implementado em versões futuras do PRESTO, permitindo um melhor escalamento dos sinogramas de dispersão e, consequentemente, contribuir para melhorar a qualidade das imagens de PET.

Palavras-chave: PET; dispersão de Compton; *scatter tails*; SSS; BrainPET; NPCD; ML; filtro *boxcar*; PI.

Abstract

Compton scattering degrades image contrast in PET, being one of the main phenomena that affects image quality. Several algorithms have been proposed to correct the data. One of the most prominent algorithms is the SSS, which provides no absolute values, but predicts the slope of the scatter distribution. This slope has to be scaled using the scatter tails as reference. However, these have very low counts, thus giving large uncertainties to determine the scatter component.

The aim of this project is to implement and evaluate new and existing scatter scaling methods, in order to improve the scaling step of the SSS.

Two scatter scaling methods were proposed (the NPCD and the ML methods) and compared with the method currently used in the data from the BrainPET scanner (Standard method). The methods were compared in a single sinogram plane and using multiple sinogram planes in combination with a boxcar filter or Plane Integration (PI). Also, different error sources were investigated in the data to test how they influence the scatter estimation and scaling. The scatter correction procedures were tested with simulated and real data.

For a single sinogram plane, both methods performed better than the Standard method. The scaling factors were calculated multiple times using the three methods and the distributions were studied. The standard deviations acquired using the proposed methods have shown a reduction of 4% (NPCD) and 13% (ML), relative to the Standard method.

The standard deviation of the ML method can be further reduced by 1% if PI is used instead of the currently used boxcar filter.

The reduction in the standard deviations of the distributions indicates that the proposed methods are more accurate.

All the scaling methods behaved in the same way with respect to errors in the data.

Keywords: PET; Compton scattering; scatter tails; SSS; BrainPET; NPCD; ML; boxcar filter; PI.

Contents

Acknowledgements	i
Resumo	iii
Abstract	vii
Notation	xi
Acronyms	xiii
List of Figures	xv
1 Introduction	1
2 Theoretical Background	3
2.1 Positron Emission	3
2.2 Interaction of Radiation with Matter	4
2.2.1 Interaction of Positrons with Matter	4
2.2.2 Interaction of Photons with Matter	5
2.2.2.1 The Photoelectric Effect	5
2.2.2.2 Compton Scattering	6
2.3 Coincidence Detection	7
2.3.1 True Events	7
2.3.2 Random Events	8
2.3.3 Scattered Events	9
2.4 PET Detectors	9
2.4.1 Photomultiplier Tubes (PMTs)	9
2.4.2 Avalanche Photodiodes (APDs)	11
2.5 PET Data Organisation	12
2.5.1 Sinograms	12
2.5.2 3D-PET	13
2.6 PET Data Correction	15
2.6.1 Normalisation	15
2.6.2 Randoms Correction	17
2.6.3 Attenuation Correction	17

2.6.4	Compton Scattering Correction	19
2.6.4.1	Energy Window-based Approaches	20
2.6.4.2	Single Scatter Simulation (SSS)	21
2.7	Image Reconstruction	24
2.7.1	Backprojection Techniques	24
2.7.1.1	Simple Backprojection	24
2.7.1.2	Filtered Backprojection	25
2.7.2	Iterative Reconstruction Algorithms	26
2.7.2.1	Maximum Likelihood Expectation Maximization (MLEM)	27
2.7.2.2	Ordered Subsets Expectation Maximization (OSEM)	28
3	Materials and Methods	29
3.1	BrainPET Scanner	29
3.1.1	Hardware	29
3.1.2	Organization of the Sinogram Files	30
3.2	Classification of the Scatter Tails	31
3.3	Standard Scaling Method	33
3.4	Non Pre-Corrected Data (NPCD) Scaling Method	34
3.5	Maximum Likelihood (ML) Scaling Method	35
3.6	Plane Integration	36
3.7	Generation of Simulated Data	37
3.8	Acquisition of Real Data	38
3.9	Evaluation of Performance	38
3.9.1	Simulated Data	38
3.9.1.1	Comparison of the Scaling Methods	38
3.9.1.2	Plane Integration <i>versus</i> Boxcar Filter	39
3.9.1.3	Evaluation of Error Sources	39
3.9.2	Real Data	41
4	Results and Discussion	43
4.1	Simulated Data	43
4.1.1	Comparison of the Scaling Methods	43
4.1.2	Plane Integration <i>versus</i> Boxcar Filter	46
4.1.3	Evaluation of Error Sources	49
4.1.3.1	Error in the Scatter Scaling Factor	49
4.1.3.2	Error in the Random Estimation	52
4.1.3.3	Use of the Reconstructed Image to Estimate the Scatter Distribution	55
4.2	Real Data	58
5	Conclusion	61
	References	63
	Index	67

Notation

A	Activity
E	Energy
E_0	Energy of the incident photon
E_B	Binding energy
E_γ	Photon energy
E_{PE}	Energy of the photoelectron
E_s	Energy of the photon scattered by a Compton interaction
$N_{i,p}$	Value of bin i in plane p of the normalisation sinogram file
P_{noise}	Simulated prompts sinogram with Poisson noise
$P_{i,p}$	Value of bin i in plane p of the prompts sinogram file
$R_{i,p}$	Value of bin i in plane p of the randoms sinogram file
S	Span
$S_{i,p}$	Value of bin i in plane p of the scatter sinogram file
$T_{1/2}$	Half-life of a radionuclide
T_{rate}	Coincidence rate of the true events
Z	Atomic Number
Ω	Solid angle
α	Scaling factor
β^+	Positron
γ	Gamma photon
λ	Expected value in a Poisson distribution
λ_d	Decay constant
n	Neutron
p^+	Proton
μ	Attenuation coefficient
ν	Neutrino
ϕ	Angle of projection (sinogram space)
σ	Klein-Nishina total cross-section
σ_{std}	Standard deviation
θ	Scatter angle of a photon in a Compton interaction
ζ	Angle formed between the LOR and the transaxial plane (3D-PET)
c	Speed of light
i_ζ	Segment number

m_e	Mass of the electron ($9.109\,382\,91 \times 10^{-31}$ kg)
p	Plane number in a sinogram file
r	Distance to the center of the scan field (sinogram space)
r_e	Electron radius
t	Time
z	Position in the axial direction (3D-PET)

Acronyms

ACF	Attenuation Correction Factor
APD	Avalanche Photodiode
CT	Computer Tomography
DEW	Dual Energy Window
ETM	Estimation of the Trues Method
FBP	Filtered Backprojection
FOV	Field-Of-View
FT	Fourier Transform
LOR	Line-Of-Response
LSO	Lutetium Oxyorthosilicate
ML	Maximum Likelihood (scaling method)
MLEM	Maximum Likelihood Expectation Maximization
MR	Magnetic Resonance
NPCD	Non Pre-Corrected Data (scaling method)
OP-OSEM	Ordinary Poisson Ordered Subsets Expectation Maximization
OSEM	Ordered Subsets Expectation Maximization
PET	Positron Emission Tomography
PI	Plane Integration
PMT	Photomultiplier Tube
PRESTO	PET REconstruction Software TOolkit
ROI	Region Of Interest
SNR	Signal-to-Noise Ratio

SSS Single Scatter Simulation

TBA Template-Based Attenuation correction

List of Figures

2.1	True event detection.	8
2.2	Random event detection.	8
2.3	Detection of a photon pair that has undergone a single scatter. . .	9
2.4	PMT scheme.	10
2.5	APD scheme.	11
2.6	Sinogram acquisition.	12
2.7	Left - 2D-PET; Middle - 3D-PET; Right - Additional parameters of 3D-PET.	13
2.8	Segments in 3D-PET ($S = 1$).	14
2.9	Michelogram.	15
2.10	Detection of two 511 keV photons.	18
2.11	Image without attenuation correction.	18
2.12	Image without scatter correction.	20
2.13	SSS algorithm.	22
2.14	Image with scatter correction.	23
2.15	Simple Backprojection.	24
2.16	General concept of the iterative reconstruction algorithms.	26
3.1	The BrainPET scanner at the Forschungszentrum Jülich.	30
3.2	Attenuation map.	32
3.3	Normalisation sinogram.	32
3.4	Tail mask (plane 1).	33
3.5	Process used to generate the tail mask.	33
3.6	Plot of the function defined in equation 3.7.	36
3.7	Phantom used for the acquisition of real data.	38
3.8	Approach taken to correct for Compton scattering without using the phantom image.	41
4.1	Distribution of the scaling factors for the ML method at different levels of statistics.	44
4.2	Distribution of the scaling factors for all the methods.	45
4.3	Bar chart of the standard deviation values.	45
4.4	Bar chart of the reduction in the standard deviation.	46
4.5	Plot of the standard deviation using the NPCD method with a boxcar filter.	47

4.6	Plot of the standard deviation using the ML method with a boxcar filter.	47
4.7	Percentage of improvement by using the NPCD method with PI instead of the boxcar filter.	48
4.8	Percentage of improvement by using the ML method with PI instead of the boxcar filter.	49
4.9	Error in the scatter scaling factor (scatter tails).	50
4.10	Error in the scatter scaling factor (sinograms).	50
4.11	Error in the scatter scaling factor (image profiles).	51
4.12	Error in the scatter scaling factor (ratio of the image profiles). . .	51
4.13	Error in the randoms estimation (scatter tails).	52
4.14	Error in the randoms estimation (sinograms).	53
4.15	Error in the randoms estimation (image profiles).	53
4.16	Error in the randoms estimation (ratio of the image profiles). . . .	54
4.17	Use of the reconstructed image to estimate the scatter distribution (image profiles using the estimations of RA image vs. phantom image).	55
4.18	Use of the reconstructed image to estimate the scatter distribution (image profiles using several iterations; 30% scatter).	56
4.19	Use of the reconstructed image to estimate the scatter distribution (image profiles using several iterations; 50% scatter).	56
4.20	Intensity differences in the ROI with the number of iterations used and for different scatter fractions (simulated data).	57
4.21	Use of the reconstructed image to estimate the scatter distribution (image profiles using several iterations; more complex phantom). .	58
4.22	Profiles of the images reconstructed with real data.	59
4.23	Intensity differences in the ROI with the number of iterations used (real data).	59

CHAPTER 1

Introduction

Positron Emission Tomography (PET) is a nuclear medicine modality which has proven to be very valuable in the diagnose of several pathologies. It uses *radiopharmaceuticals* (also known as *tracers*) with short half-life radionuclides in order to obtain an emission image, such as: ^{11}C , ^{13}N , ^{15}O and ^{18}F [Bronzino, 2000].

The tracer is metabolised at different rates by the different tissues. Therefore, the acquired image will be a functional image. This phenomenon is specially important in cancer diagnosis, since cancer cells have a higher uptake than normal cells, due to their higher metabolism. Note that different tracers have different properties and are used for different tasks, cancer diagnosis is only one of them.

As the name states, PET relies on positron emission by the radionuclides. Each positron will in turn annihilate with an electron producing two 511 keV γ photons, which are detected by the PET system and used to reconstruct an image showing the tracer concentration.

The image quality is influenced by many factors, one of the most important ones is Compton Scatter, which leads to the deterioration of image contrast. The phenomenon itself and the reason behind the negative effect will be further explained in section 2.3.3.

It is possible to estimate the amount of scatter in a PET image and to correct for it. Indeed, several approaches have been proposed to correct for this effect, such as: Energy Window-based Approaches and Single Scatter Simulation (SSS). The details will be explained in section 2.6.4.

The SSS algorithm provides an accurate estimation of the scatter distribution. However, the distribution is not scaled to the measured data, this has to be done in a separate step. The scaling step is essential in order to ensure that the amount of scatter that is corrected for is as close as possible to the amount of scatter in the data.

At the Forschungszentrum Jülich, the scaling of the scatter distribution estimated from the data acquired with the BrainPET scanner is performed by the software packages provided by Siemens.

The aim of this project is to implement and evaluate new and existing scatter scaling methods, in order to improve the scaling step in the SSS algorithm.

Chapter 2 will introduce the basic physical concepts along with the procedures used to correct and reconstruct PET images.

Chapter 3 will be focused on a more detailed description of the BrainPET system at the Forschungszentrum Jülich, the implemented scatter scaling methods and the procedures used to simulate and acquire data. This chapter will also describe the tests performed with these data.

Chapter 4 will present the results acquired in all the tests and their respective discussion.

Finally, an overview of the conclusions and future prospects will be presented in chapter 5.

Theoretical Background

In order to understand how scatter correction works, one must first understand the basic principles of PET imaging.

This chapter will start by giving an overview of the physical processes involved in PET imaging, namely, positron emission (section 2.1) and the interaction of radiation with the medium (section 2.2). Then, the types of events that are detected by PET systems will be described in section 2.3.

The types of detectors that are used will be mentioned in section 2.4 and the data organisation in 2D-PET and 3D-PET will be explained in section 2.5. Then, the strategies used for data correction will be described in section 2.6.

Finally, after the data is acquired and corrected, it needs to be reconstructed. Section 2.7 will make an overview of the most important image reconstruction methods in PET.

2.1 Positron Emission

PET relies on the administration of a tracer to the patient which is metabolised differently by the tissues.

The tracer molecule contains a specific radionuclide, which consists of a nucleus in an unstable state. This tends to release energy in order to reach a more stable state. One of the processes by which this release of energy can occur is through *positron emission*. In such a process, a proton (p^+) in the unstable nucleus is converted into a neutron (n) by emitting a positron (β^+) and a neutrino (ν) [Cherry et al., 2003]:



The phenomenon described in equation 2.1 is called *positron decay*, and the rate at which it occurs is expressed by the *activity*.

Considering a sample of N nuclei, the average decay rate is given by:

$$\frac{\Delta N}{\Delta t} = -\lambda_d N \quad (2.2)$$

where λ_d is the *decay constant*. This is characteristic for each radionuclide. It is equal to the average fraction of nuclei that decay per second. The activity A of the sample is given by the absolute value of the average decay rate (equation 2.2) and is expressed in *Becquerel* [Bq]:

$$A = \left| \frac{\Delta N}{\Delta t} \right| = \lambda_d N \quad (2.3)$$

As one can see by equation 2.3, the activity depends on the number of nuclei, thus, it decreases with the time. This can be written as:

$$A(t) = A(0) e^{-\lambda_d t} \quad (2.4)$$

where $A(0)$ is the initial activity and $e^{-\lambda_d t}$ is the *decay factor* [Cherry et al., 2003].

Usually, radionuclides are characterised by their *half-life* $T_{1/2}$, which is equal to the time necessary for 50% of the nuclei to decay. This can be calculated using the following formula:

$$T_{1/2} = \frac{\ln(2)}{\lambda_d} \quad (2.5)$$

2.2 Interaction of Radiation with Matter

There are different ways of interaction between radiation and matter. In PET imaging the main focus lies in the interaction of *charged particles* with matter and in the interaction of *electromagnetic radiation* with matter. These shall be further explained in sections 2.2.1 and 2.2.2.

2.2.1 Interaction of Positrons with Matter

The positron (β^+) is a charged particle with the same mass as the electron but with a positive charge. Charged particles lose energy by interactions with atoms and molecules of the medium. These can be divided into three types.

1. **Ionization:** When a charged particle passes close enough to an electron cloud, it can cause the ejection of an electron, thus, *ionizing* the atom. In this interaction, the incident charged particle transfers some energy to the electron. Part of this energy is used to overcome the binding energy of the electron to the atom. The rest is used as kinetic energy by the ejected electron. These electrons are called *secondary electrons* and, if they have enough energy, they can cause *secondary ionizations*. In this case, the secondary electron is called a δ ray [Cherry et al., 2003].

2. **Excitation:** If a charged particle passes further way from the atom, it causes the excitation of the atom without ionization. This interaction usually involves a smaller energy transfer when compared with the previous one [Cherry et al., 2003].
3. **Interaction with the nucleus:** In this case, the particle is deflected and decelerates due to the strong electric field, releasing energy in the form of electromagnetic radiation called *Bremstrahlung* [Cherry et al., 2003].

Since positrons have a small mass, they can suffer large deflections upon interacting with the atoms of the medium. Therefore, their trajectories are more irregular when compared with heavier charged particles. Upon being emitted, a positron will travel a small distance inside the medium (in the order of a few millimeters) losing its kinetic energy. Finally, it will interact with an electron from the medium, causing the mass of both particles to be converted into energy. This process is called *annihilation* and it results in the emission of two 511 keV *annihilation photons*. Due to the conservation of momentum, the photons travel in opposite directions. However, since both particles are not exactly stationary upon their interaction, some small deviation from the perfect 180° difference occurs [Cherry et al., 2003].

The non-collinearity of the annihilation photons and the positron range are two physical factors that limit the spatial resolution of PET [Shibuya et al., 2007].

2.2.2 Interaction of Photons with Matter

After the annihilation γ photons are produced. These can be detected by the PET system. However, before reaching the detectors, they can interact with the medium due to different processes. In the following subsections the most relevant interactions will be explained: the photoelectric effect and Compton scattering.

2.2.2.1 The Photoelectric Effect

In a photoelectric interaction, a photon is absorbed by an atom which in turn ejects an electron, known as a *photoelectron*, with kinetic energy equal to:

$$E_{\text{pe}} = E_0 - E_{\text{B}} \quad (2.6)$$

E_{pe} denotes the kinetic energy of the photoelectron, E_0 is the energy of the incident photon and E_{B} is the binding energy to the shell from which the photoelectron is ejected. Thus, the photoelectric effect only occurs when the energy of the incident photon is greater than the binding energy of the electron.

When an electron from an inner shell is ejected from the atom, a vacancy is formed. This can be filled by an electron from an outer shell, which results in the emission of a characteristic X-ray with an energy equal to the energy difference between the shells. If the shell from which the electron came is not the valence shell, then, the vacancy left by this electron can be filled by another electron

accompanied by the emission of another characteristic X-ray. The process can be repeated, originating an *electron cascade*, with the emission of a cascade of characteristic X-rays [Bushberg et al., 2002].

The transition of an electron from an outer shell to an inner shell does not always result in the emission of a characteristic X-ray. A phenomenon can occur in which a second electron from the outer shell is ejected, leaving two vacancies in the outer shell. This electron is known as an *Auger electron* [Turner, 2007].

The probability of occurrence of a photoelectric interaction is dependent on the atomic number Z of the medium and the photon energy E_γ [Bushberg et al., 2002]. It can be written as:

$$P_{\text{PE}} \propto \left(\frac{Z}{E_\gamma} \right)^3 \quad (2.7)$$

This relation is very important when choosing the scintillation crystals of a PET system (section 2.4.1).

2.2.2.2 Compton Scattering

Unlike in the case of the photoelectric effect, Compton scattering denotes the interaction of a photon with an electron from an outer shell, leading to the transfer of energy to the electron and scatter of the photon with a certain angle. The energy of the scattered photon is given by the following formula:

$$E_s = \frac{E_0}{1 + \frac{E_0}{m_e c^2} (1 - \cos \theta)} \quad (2.8)$$

where E_0 is the energy of the incident photon, m_e is the mass of the electron, c is the speed of light in the vacuum and θ is the *scatter angle*.

According to equation 2.8, the amount of energy transferred increases with the scatter angle, reaching a maximum at 180° (*back-scatter*).

The probability of a photon being scattered in a certain direction is given by the Klein-Nishina equation:

$$\begin{aligned} \frac{d\sigma}{d\Omega} = & \frac{r_e^2}{2} (1 + \cos^2 \theta) \left[\frac{1}{1 + \frac{E_0}{m_e c^2} (1 - \cos \theta)} \right]^2 \\ & \left[1 + \frac{\left(\frac{E_0}{m_e c^2} \right)^2 (1 - \cos \theta)^2}{\left[1 + \frac{E_0}{m_e c^2} (1 - \cos \theta) \right] (1 + \cos^2 \theta)} \right] \end{aligned} \quad (2.9)$$

where $d\sigma/d\Omega$ is the differential scattering cross-section, r_e is the electron radius and θ is the scatter angle [Zaidi and Koral, 2006]. This equation is very important in model-based scatter correction algorithms, such as, the Single Scatter Simulation (SSS) (section 2.6.4.2).

2.3 Coincidence Detection

Photon pairs coming from the positron-electron annihilation are counted in several detector rings. The detected pairs are referred to as *prompt events*, which are subdivided into: *true events*, *random events* and *scattered events* [Valk et al., 2003]. These shall be explained in more detail in the next sections.

The detected prompts follow a *Poisson distribution*. In this distribution, for an expectation value of λ and a measured value of k events, the probability $P(X = k)$ to obtain k events can be written as:

$$P(X = k) = \frac{\lambda^k e^{-\lambda}}{k!} \quad (2.10)$$

where $\lambda \in \mathbb{R}^+$ and $k \in \mathbb{N}_0$.

This property of the prompts means that a PET image is affected by *Poisson noise*. This type of noise is characterised for being signal dependent, which means that its influence is dependent on the amount of counts in an image. In fact, the Signal-to-Noise Ratio (SNR) in a certain region of an image corrupted by Poisson noise is proportional to the mean photon count in that region. The consequence of this property is that images with higher counts will be less influenced by noise than images with lower counts [Wernick and Aarsvold, 2004].

2.3.1 True Events

The γ photons travelling in opposite directions will be detected by a detector pair. In figure 2.1, the photon pair emitted by a positron annihilation within the body of the patient is detected by the detectors *A* and *B*. When the first photon of the pair is detected, there is a *timing window* in which the system will accept the arrival of the second photon. If no second photon is detected within this time, the system rejects this single event. The timing window is around a few nanoseconds (typically from 2–10 ns) and its duration is limited by the temporal resolution of the electronic components of the PET scanner.

If the two paired photons are detected within the same timing window, it is possible to draw a Line-Of-Response (LOR) between the two detectors, meaning that the annihilation has occurred somewhere along that line. An event is said to be a true event if two photons coming from the same annihilation are unscattered and detected within the same timing window.

By detecting multiple LORs, one can reconstruct an image from the emitted γ photons.

One fact that must be taken into account when viewing these images, is that the positrons will travel a few millimetres before annihilating with an electron (section 2.2.1). Thus, the defined LOR is related to the location where the positron-electron annihilation occurred, and not to the location where the positron emission took place. This limits the resolution to the distance travelled by the positron, being one of the factors that contributes to image blurring [Cherry et al., 2003].

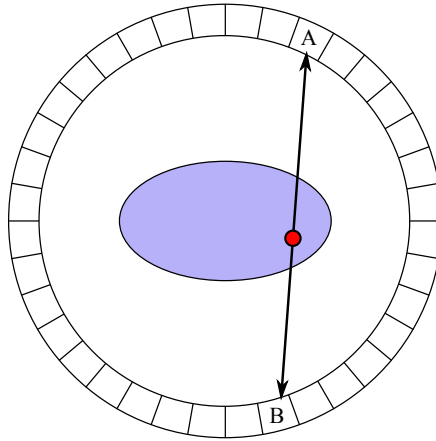


Figure 2.1: True event detection.

2.3.2 Random Events

There are some cases in which a photon from another annihilation is detected within the same timing window instead of the true photon, originating a random count (figure 2.2).

Considering the case in figure 2.2, the photon pair from the annihilation on the right should be detected by the detectors *A* and *B*. However, the photon reaching detector *A* is not detected due to detector inefficiency. Another annihilation occurs at proximately the same time in which the photons should be detected by the detectors *C* and *D*, but the photon reaching detector *D* is not detected. If the photon heading for detector *C* is detected within the timing window of detector *B*, the system will consider that an annihilation has occurred along the line \overline{BC} and define that LOR, even though it does not represent the correct location of the radioactive nuclide.

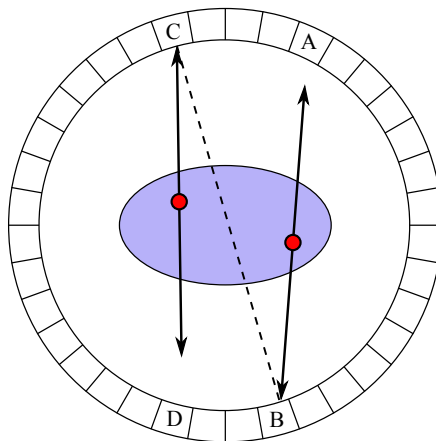


Figure 2.2: Random event detection.

In other cases, two or more photons can be detected within a timing window. This is called a *multiple coincidence* detection and is ignored by the system.

2.3.3 Scattered Events

The emitted γ photons can interact with matter before being detected. There are a number of different phenomena by which this interaction can occur. Compton scattering is a very common interaction that can strongly degrade image quality.

In case of scattering, a scattered photon can be detected by a detector leading to an incorrect LOR (figure 2.3), which results in a loss of contrast. This LOR can even cross regions in space where there is no activity, such as, outside a patient [Zaidi and Montandon, 2007].

Scattered events are not limited to the single scatter case, in which one of the photons is scattered just once before being detected (as represented in figure 2.3). In some cases, both photons in a photon pair can be scattered, also, each photon can be scattered more than once.

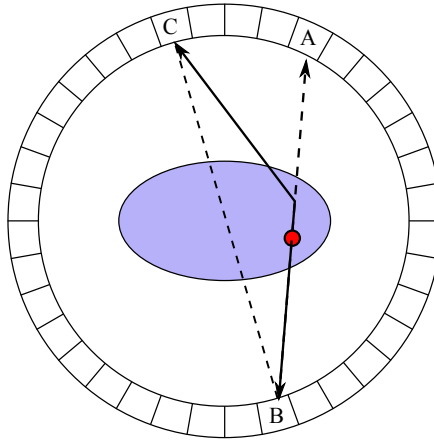


Figure 2.3: Detection of a photon pair that has undergone a single scatter.

For appropriate data correction, the estimation of the background of scattered events is essential. Therefore, different techniques can be used. These are further explained in section 2.6.4.

2.4 PET Detectors

This chapter will begin by describing one of the most common detectors used in PET systems, the *Photomultiplier Tube* (PMT). Then, this will be compared with another detector which is used in PET/MR systems due to its insensitivity to magnetic fields, the *Avalanche Photodiode* (APD).

2.4.1 Photomultiplier Tubes (PMTs)

PMTs are the components in PET scanners which are responsible for detecting γ photons by converting the optical signal into an electric signal and amplifying it.

Several PMTs are coupled with a scintillation crystal forming a *detector block*. The crystal absorbs the incident γ photon by photoelectric effect (section 2.2.2.1).

Since the probability of a photoelectric effect occurring increases with the atomic number Z (equation 2.7), the crystals used have a high Z in order to absorb the incoming photons. The most commonly used crystals are: bismuth germanate (BGO), gadolinium silicate (GSO) and lutetium oxyorthosilicate (LSO) [Suetens, 2009].

The photoelectron resulting from the photoelectric absorption will collide with other electrons of the medium. This will release energy in the form of photons with a frequency within the visible range called *scintillation photons*. The amount of photons produced is dependent on the energy of the incident γ photon.

The scintillation photons will be absorbed in the photocathode by photoelectric effect and the resulting photoelectrons will be accelerated to the first dynode due to a difference in electric potential. They will hit the dynode with a greater kinetic energy, resulting in the emission of more electrons which will be accelerated to the next dynode (figure 2.4).

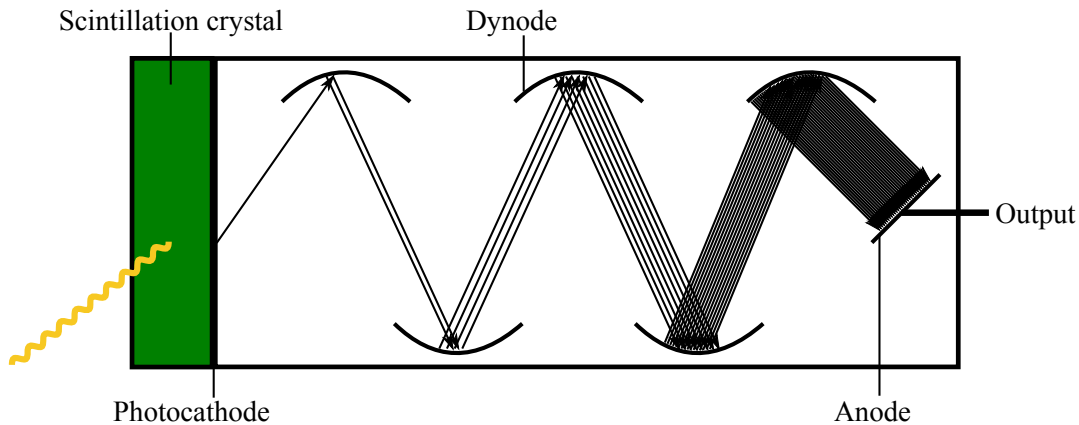


Figure 2.4: Scheme of a PMT amplifying the electric signal resulting from the detection of a single γ photon.

Since each dynode has an electric potential greater than the previous one, the electrons will hit each one of the dynodes, increasing the amount of electrons until they are detected in the anode (figure 2.4). The mean number of electrons collected by the anode can be written as:

$$\langle N \rangle = g^n \quad (2.11)$$

where g is the amount of electrons that leave the first dynode and n is the number of dynodes in the PMT [Akay, 2006].

The main reasons for using PMTs in PET are their high gain and the ability to measure the energy of the incident γ photon (which is related to the intensity of the output signal).

2.4.2 Avalanche Photodiodes (APDs)

When the first efforts were made to join the modalities of PET and Magnetic Resonance (MR), one of the first issues was with the PET detectors.

The PMTs rely on the acceleration of electrons between several dynodes (section 2.4.1). These electrons are deflected by strong magnetic fields, which means that the PMTs will not work properly in the strong magnetic fields used in MR. Therefore, they need to be substituted by another kind of detectors.

Hybrid PET/MR systems can use APDs instead of the PMTs because they are insensitive to magnetic fields. These are very sensitive photodiodes in which a reverse voltage is applied. They are composed of a positive doped region (**p**) and a negative doped region (**n**) with a neutral region between them (figure 2.5) [Ham].

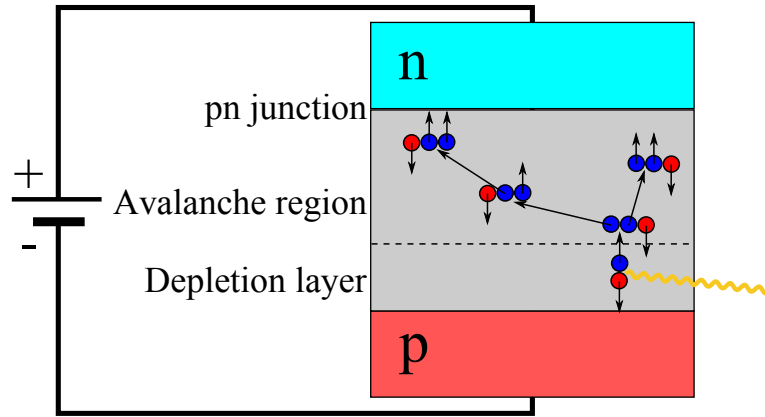


Figure 2.5: Scheme of a APD amplifying the signal resulting from the detection of a scintillation photon.

Like in the case of the PMTs, multiple APDs are coupled with a scintillation crystal which produces scintillation photons. When a scintillation photon arrives at the APD, it interacts with the medium in the depletion layer, forming an electron-hole pair. These will drift towards opposite regions of the APD, due to the applied electric field. The electrons that are produced in the depletion layer will ionize other atoms in the avalanche region, producing more electrons (figure 2.5) [Ham, 2004]. This is known as *avalanche effect*.

The avalanche effect allows the APDs to achieve a very high gain (~ 200). This makes them very useful in applications where a high sensitivity is needed. However, they present some drawbacks. Among these are the dependence of the gain on the temperature and the greater amount of noise [Akay, 2006, Ham, 2004].

2.5 PET Data Organisation

After the events are detected, the data need to be sorted. This section will start by covering the basic concepts of data organisation in 2D-PET (section 2.5.1), and then extend these concepts to 3D-PET (section 2.5.2).

2.5.1 Sinograms

When a detector pair measures a coincidence, the LOR is defined between the two detectors, meaning that the annihilation has occurred somewhere along that line. The system cannot determine its exact position by taking just one measurement. Therefore, multiple LORs are needed to acquire enough data to reconstruct the image of the activity distribution.

In order to organise and use the acquired projection data, a more convenient system of coordinates is necessary. In 2D-PET, each LOR is defined by two parameters: the distance to the centre of the scan field (r) and the angle of projection (ϕ). Each LOR in figure 2.6-A corresponds to a bin in a *sinogram* (figure 2.6-B). Therefore, all events coming from the same LOR will be added to the same bin [Fahey, 2002, Saha, 2005]. In other words, each point in the coordinate space (r, ϕ) represents a LOR in the (x, y) coordinate space [Cherry et al., 2003].

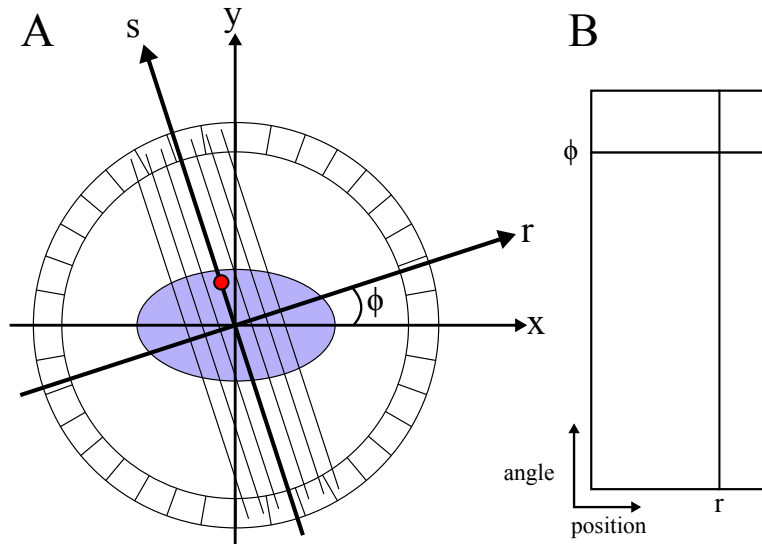


Figure 2.6: Sinogram acquisition; A - Detection of an event; B - The information is stored in the sinogram bin with the parameters corresponding to the LOR of the detected event (r, ϕ) .

After the LOR data is sorted into sinograms, these can be used to reconstruct the image of the object using different algorithms. These shall be explained in section 2.7.

2.5.2 3D-PET

Current PET scanners have more than one detector ring. This allows the acquisition of more than one plane simultaneously. In order to reduce the scattered counts, some PET scanners have septa localized between the rings. An acquisition with this configuration is known as an acquisition in 2D-mode. Generally, this allows only events from the same ring or from adjacent rings to be counted (figure 2.7). Thus, a scanner with N rings will have N sinograms from direct planes and $N - 1$ sinograms from cross planes, which equals a total of $2N - 1$ sinograms [Saha, 2005].

In the 3D-PET modality, the septa are removed, increasing the number of counts acquired for each plane, by allowing more events to be measured than just the ones in the same detector ring and in adjacent detector rings (figure 2.7). If a scanner has N rings then, since all ring combinations are allowed, the number of sinograms should be equal to N^2 . Usually, data compression is applied, which means that the number of sinograms will not be that high. However, the number of combinations allowed is still higher than in 2D-PET [Fahey, 2002]. This will significantly increase the sensitivity of the system at the expense of an increase in the detection of scattered and random events [Fahey, 2002, Saha, 2005]. The amount of scatter in 2D-PET is around 10%–15% [Fahey, 2002]. However, scatter constitutes 20–50%+ of the data in 3D-PET [Valk et al., 2003]. Therefore, scatter correction techniques play an even more important role in 3D-PET.

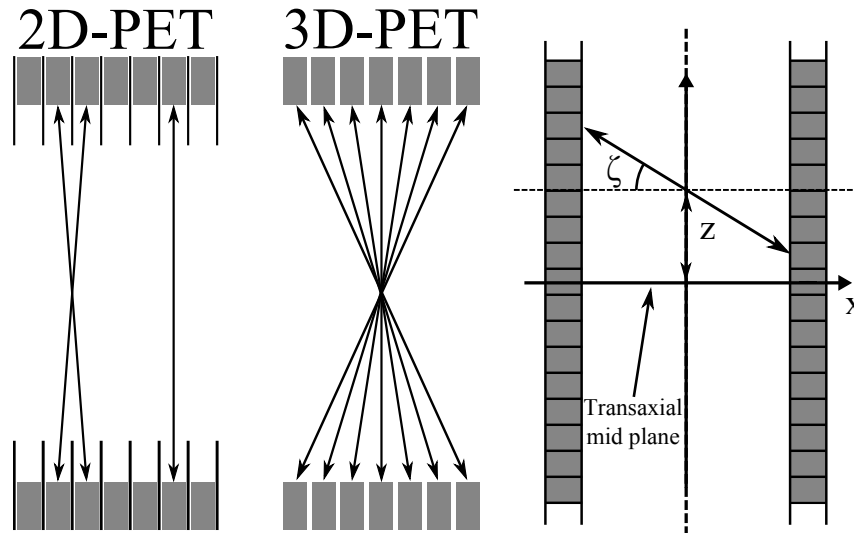


Figure 2.7: Left - 2D-PET; Middle - 3D-PET; Right - Additional parameters of 3D-PET.

The LORs in 3D-PET are represented by four parameters. These are the two parameters used in 2D-PET (r, ϕ), plus two new parameters: z and ζ (figure 2.7). The former is the position along the axial direction relative to the transaxial mid-plane and the latter is the angle formed between the LOR and the transaxial plane [Martins, 2007].

This 3D information is usually organised in groups called *segments*. As one can see in figure 2.8, the sinograms can be classified by the ring combination. Note, that for the same combination of two rings there are two sinograms, the organisation of the events in these two sinograms depends on the detector combination.

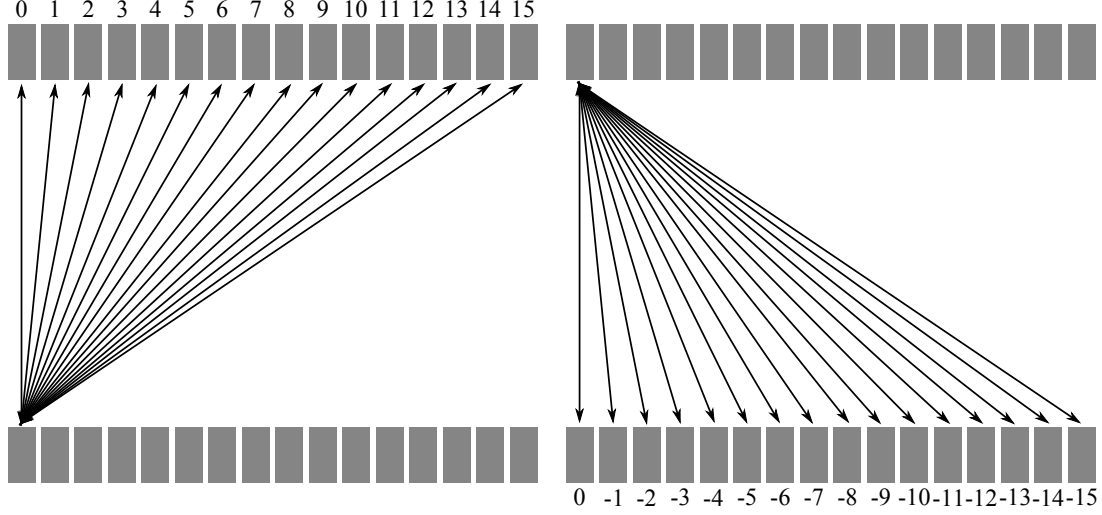


Figure 2.8: Segments in 3D-PET ($S = 1$).

In order to save storage space, some scanners use axial angular undersampling by combining sets of sinograms with adjacent values of ζ . The degree of undersampling is characterized by an odd integer called *span* [Valk et al., 2003].

Considering two detector rings with ring numbers R_A and R_B , the events detected between these will belong to segment i_ζ if the following condition is met:

$$i_\zeta S - S/2 \leq R_B - R_A \leq i_\zeta S + S/2 \quad (2.12)$$

where S is the span.

The organization of the compressed data can be represented in a *Michelogram*. Figure 2.9 shows a Michelogram of a scanner with 16 rings and a span of 5. Each ring combination is represented as a point in the grid and each sinogram is represented as a line segment connecting all the contributing ring pairs.

In a PET scanner, the amount of sinograms per segment decreases with the absolute value of the segment number. This can be seen in figures 2.8 and 2.9.

In figure 2.8, there is no data compression in the axial direction ($S = 1$). One can see that segment 0 has 16 sinograms (direct detector combinations from ring 0 to ring 15), while segments -15 and 15 only have 1 sinogram each, since it is not possible to combine any other detectors with such a large ring difference. The total number of sinograms in this case is 256.

Figure 2.9 shows the organization of the data coming from the scanner in figure 2.8, but with the use of axial data compression ($S = 5$). The number of segments in this case is lower than with $S = 1$. However, the number of sinograms per segment is different, e.g. segment 0 has 31 sinograms instead of 16. The use

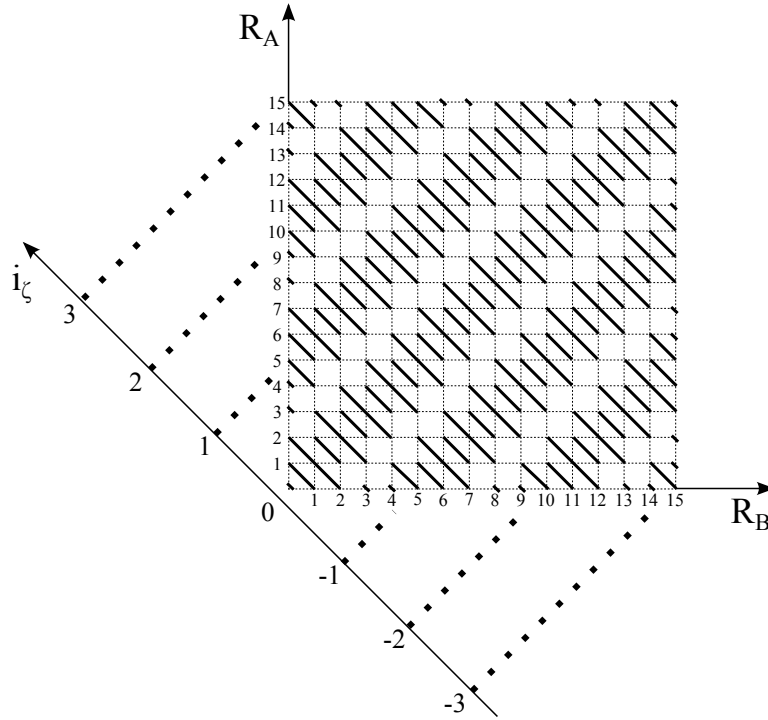


Figure 2.9: A Michelogram corresponding to a PET scanner with 16 rings and with $S = 5$. Image adapted from Valk et al. [2003].

of axial data compression also decreases the total number of sinograms. In this case, the total number of sinograms is 121.

2.6 PET Data Correction

Data acquisition in PET is compromised by multiple effects. Thus, data correction is essential before an image can be reconstructed. The following sections will explain the basis of the different corrections used in PET.

2.6.1 Normalisation

During a PET measurement, not all the emissions are detected, even if both photons hit the scintillation crystals within the timing window. One of the things that has to be considered is the sensitivity of the system, which characterises the probability to detect coincidence events. The sensitivity is influenced by both geometrical effects and detector efficiencies. This means that it is not the same for all the LORs.

There are many geometrical effects that have to be taken into account, some of the most important are data compression and the geometric and solid angle effects [Valk et al., 2003]. The former consists in the grouping of several physical LORs in order to reduce the amount of data (section 2.5.2) and the latter is related to the incidence angle of the photons in the scintillation crystals.

If a photon enters a scintillation crystal at a certain angle, it can cross more material than a photon that enters perpendicularly to the crystal surface. Thus, it is more likely that it will interact. This means that the sensitivity will vary with the radial position (r) of the LOR. However, a photon entering a crystal close to its edge and with a certain angle can encounter less material in its path, making it more likely to escape without being detected. Therefore, the sensitivity will vary with the radial position and the position of the LOR relative to the crystals [Valk et al., 2003].

The variation of the detector efficiency can be due to several factors. These include physical differences between the crystals, differences in the gains of the detectors and differences in the position of the detector elements in a detector block.

The variation of the sensitivity means that the activity coming from the same point in space will have different detection probabilities depending on the detector pair. These variations can give rise to artefacts in the reconstructed image. Thus, they must be corrected by using a procedure called *normalisation*. In this section, two types of normalisation procedures will be explained: *direct normalisation* and *component-based normalisation*.

The direct normalisation involves using a known distribution to record the amount of counts detected by all detector pairs [Oakes et al., 1998]. The normalisation factor for each detector pair (i, j) is computed as:

$$N_{i,j} = \frac{\langle C_{i,j} \rangle}{C_{i,j}} \quad (2.13)$$

where $C_{i,j}$ is the number of counts in the detector pair (i, j) and $\langle C_{i,j} \rangle$ is the expected number of counts in the same detector pair [Cherry et al., 2003]. The counts measured during an acquisition can then be corrected as follows:

$$P'_{i,j} = P_{i,j} \times Norm_{i,j} \quad (2.14)$$

where $P_{i,j}$ corresponds to the measured prompts and $P'_{i,j}$ to the normalised prompts.

One of the disadvantages of this method is that it requires scan times of several hours [Valk et al., 2003]. In order to reduce these, one can use component-based normalisation instead of direct normalisation.

The component-based normalisation consists in the use of a model to estimate the normalisation factors. In this model, the contributions of the different components that affect the sensitivity are determined separately. However, a typical protocol to acquire the necessary data involves only two measurements: a rotating rod source and a uniform cylinder source. The former is used to calculate the geometric effects, while the latter is used to calculate the crystal efficiencies [Valk et al., 2003]. However, the protocols for these measurements can be different, for example, at the Forschungszentrum Jülich a rotating plane source is used instead of the uniform cylinder [Scheins et al., 2011].

2.6.2 Randoms Correction

The PET system uses a timing window in order to detect photon pairs. However, two photons coming from two different annihilations can be detected within the same timing window. Thus, one needs to have a method to estimate the fraction of random events in the prompt window.

One simple way of solving this problem is by delaying the timing window to detect random events only. For example, instead of using a 12 ns timing window starting from the moment that the first photon was detected, one can use one that starts at 64 ns and goes until 76 ns. Since a true event or a scattered event arrive to a detector pair within the first 12 ns, only random events will be detected using this window. Thus, the rate of random events detected using this window is the same as the rate detected using the 12 ns timing window [Cherry et al., 2003].

After the amount of random events has been estimated for each LOR, this information can be converted into sinograms (*randoms sinograms*) and used to correct the prompt data. One straightforward way to do this would be to subtract the data in the randoms sinograms from the prompts sinograms. However, this can cause some bins to have negative values. To avoid this, one can set the negative values to 0 or use a more advanced image reconstruction algorithm, like the Ordinary Poisson Ordered Subsets Expectation Maximization (OP-OSEM). This will not be explained in this thesis. For more information, please refer to Velden et al. [2009].

The random correction will increase the amount of statistical noise. If N_{trues} is the number of true counts, $N_{\text{scattered}}$ is the number of scattered events and N_{randoms} is the amount of subtracted random events, the uncertainty of the remaining events can be represented as [Cherry et al., 2003]:

$$\sigma_{\text{std}}(N_{\text{trues}} + N_{\text{scattered}}) = \sqrt{(N_{\text{trues}} + N_{\text{scattered}}) + (2 \times N_{\text{randoms}})} \quad (2.15)$$

2.6.3 Attenuation Correction

When the annihilation photons are emitted, they travel a certain distance before they reach the detectors. During this time, they may interact with the atoms of the medium and can be absorbed or scattered without being detected. This is known as *attenuation*.

Considering the case represented in figure 2.10, the photons emitted from the source represented as a red circle will travel in opposite directions to detectors *A* and *B*. However, one or both of photons might not reach the detectors if they suffer a Compton scatter with a large angle or a photoelectric absorption (section 2.2.2). The probability of both photons reaching the detectors can be written as:

$$P_{\text{det}} = e^{-\mu x} \times e^{-\mu(L-x)} = e^{-\mu L} \quad (2.16)$$

where μ is the attenuation coefficient of the medium, L is the thickness of the object and x is the distance between the source and the surface of the body (the attenuation coefficient of the air will be considered to be 0 cm^{-1}).

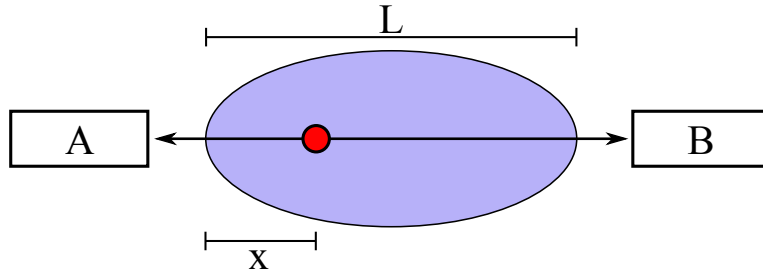


Figure 2.10: Detection of two 511 keV photons by detectors A and B . The medium where the annihilation occurred is considered to be uniform with an attenuation coefficient of μ . The attenuation coefficient of the air is considered to be 0 cm^{-1} .

One can see by equation 2.16 that the higher the attenuation coefficient (μ) and the thicker the object, the less likely will be the detection of both photons. In a PET measurement, the photons travel through tissues with varying thickness and attenuation coefficient. Thus, the probability of a photon pair being detected will depend on the position of the annihilation site. Therefore, equation 2.16 will have to be rewritten as:

$$P_{\text{det}} = e^{-\sum_{i=0}^n \mu_i L_i} \quad (2.17)$$

where n is the number of tissues, μ_i is the attenuation coefficient of the i^{th} tissue and L_i is the thickness of the i^{th} tissue [Saha, 2005].

One of the most prominent effects in PET images uncorrected for the attenuation is the representation of a lower activity coming from the interior of the body. This is due to the fact that the photons that are emitted from the centre have to go through a larger portion of tissue before reaching the detector, thus, having a higher probability of being attenuated. This effect can be seen in figure 2.11, where the intensity in the centre is lower than the intensity in the borders. The low amount of activity in the region outside the cylinder is due to scatter. This will be further explained in section 2.6.4.

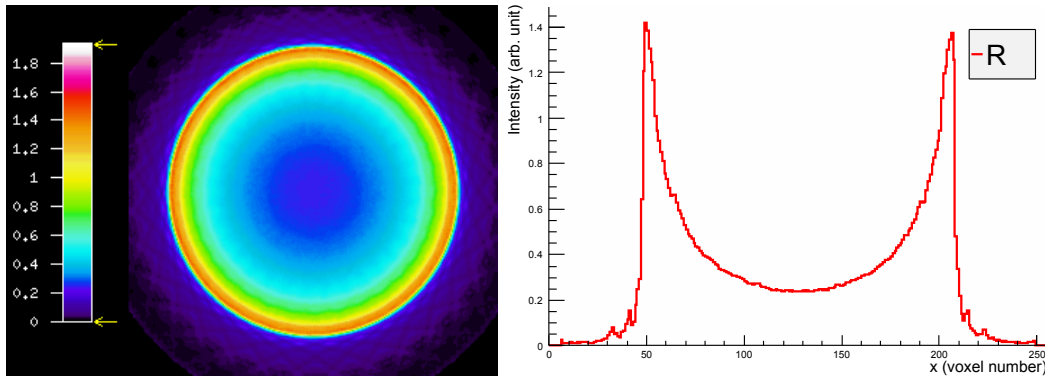


Figure 2.11: Left - Simulated uniform cylinder without attenuation correction. The image was corrected for random events and reconstructed using OP-OSEM with 8 iterations and 2 subsets; Right - Intensity profile; The simulated data were acquired following the procedure described in section 3.7.

The attenuation can be corrected in PET/CT by using the CT image to generate an *attenuation map*, which represents the amount of attenuation experienced by the 511 keV γ photons in each region of the PET image. However, in a standalone PET system, this option is not available.

One of the ways to correct for this effect, without using a CT image, is to use the *transmission scan*. This consists in the rotation of a rod with a positron source around the detector ring exposing all the detectors uniformly (*blank scan*). Then, the patient is inserted in the scanner and the measurement is repeated. The Attenuation Correction Factors (ACFs) for each detector pair are calculated as:

$$\frac{I_0}{I} = e^{\sum \mu_i L_i} \quad (2.18)$$

where I_0 is the data acquired in the blank scan and I is the data acquired with the patient in the scanner. The correction factors are then applied to each LOR of the patient measurement [Saha, 2005].

The blank scan does not need to be performed at each patient measurement. The same I_0 data can be used to correct images from several patients.

In the case of the BrainPET scanner, it is not possible to acquire a transmission scan. Since the system is used to perform PET/MR, the estimation of the attenuation map is performed using a MR image. There are several ways in which this can be done. At the Forschungszentrum Jülich, the procedure used is called *Template-Based Attenuation correction* (TBA) [Rota Kops and Herzog, 2007].

The TBA is divided into several steps. The first consists in obtaining a set of patient transmission scans. Then, these scans are normalised and averaged. MR scans of the same patients are also acquired and a similar process applied. This results in the generation of a MR template and an attenuation template.

In order to correct for attenuation in a patient image from the BrainPET scanner, the MR template is normalised to the MR image of the patient. Then, the spatial transformations applied to the MR template are applied to the attenuation template. Finally, the head holder is added to the spatially transformed attenuation template, which is then used as the attenuation map [dos Santos Ribeiro, 2012, Rota Kops and Herzog, 2007].

2.6.4 Compton Scattering Correction

Compton scattering in a PET acquisition leads to incorrectly defined LORs which will be responsible for overestimating the number of counts in certain regions of the image, resulting in the decrease of image contrast and affecting activity quantification.

If the image represented in figure 2.11 is corrected for attenuation (but not for Compton scattering), the image in figure 2.12 is obtained. This generated image is clearly affected by Compton scattering, which can be identified by two characteristics:

- Activity is observed outside the cylinder, despite the fact that there is no tracer present in that region. The counts in this region are known as *scatter*

tails and are used as a reference by the SSS algorithm (section 2.6.4.2).

- The activity in the centre of the cylinder is higher when compared to the activity close to the borders. Since the cylinder has a uniform activity distribution, this is attributed to the greater amount of scatter present in the centre of the cylinder.

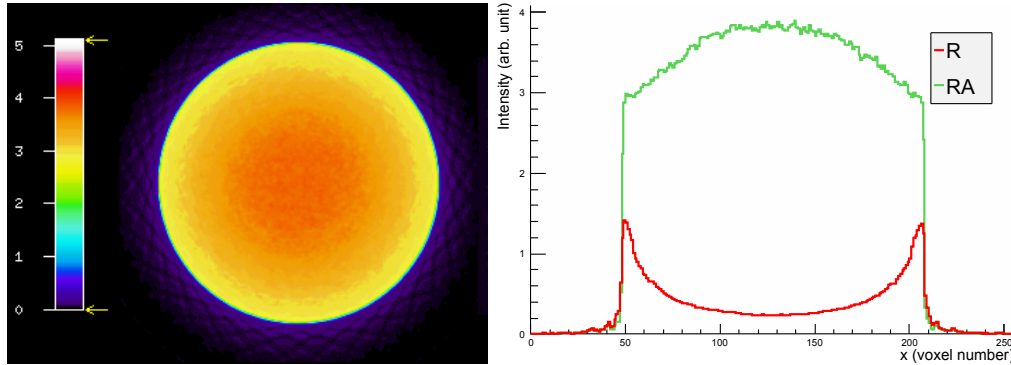


Figure 2.12: Left - Simulated uniform cylinder without scatter correction but with attenuation correction. The image was corrected for random events, attenuation effect and reconstructed using OP-OSEM with 8 iterations and 2 subsets; Right - Intensity profiles. The R profile corresponds to the one in figure 2.11. The RA profile corresponds to the image on the left; The simulated data were acquired following the procedure described in section 3.7.

Two of the most important approaches to correct for Compton scattering will be explained in the following sections: Energy Window-based Approaches and Single Scatter Simulation. However, there are other methods besides these [Bergström et al., 1983].

2.6.4.1 Energy Window-based Approaches

One of the approaches to correct scatter is to use methods based on photon energy. As explained in section 2.2.2.2, in a Compton interaction, the higher the energy transferred from the photon to the electron, the higher will be the scatter angle. Therefore, photons that suffered a Compton scatter will arrive at the detector with a lower energy than 511 keV. This phenomenon is the basis for these methods.

One option is to use two energy windows. Within this approach, there are two variants: the Dual Energy Window (DEW) technique and the Estimation of the Trues Method (ETM) [Bendriem et al., 1994, Zaidi and Koral, 2006].

In the DEW technique, two windows are defined: a higher energy window (e.g. from 380 keV to 850 keV) and a lower energy window (e.g. from 150 keV to 380 keV). It is assumed that both windows contain scattered and unscattered events [Grootoonk et al., 1996, Zaidi and Koral, 2006]. The unscattered events in the lower energy window come from photons that either deposit part of their

energy on the detector crystals, or undergo scatter in the gantry and side-shielding of the PET scanner [Grootoonk et al., 1996].

Some scaling parameters are estimated by experimental procedures with phantoms. These are used with the acquired data in order to solve two equations which allow the estimation of the unscattered component. For more information about scatter correction in 3D-PET using the DEW method, please refer to the paper by Grootoonk et al. [1996].

The ETM uses one window with a lower energy threshold above 511 keV and a regular acquisition window that also includes the previous one. This means that both windows will have the same upper energy threshold. The method considers that the number of counts recorded in each window depends on the settings of the window and on the incidence angle of the photon. Thus, the unscattered events in the higher window can be related to the ones in the wider window through a function. By doing this, one can calculate the amount of unscattered events in the wider window and remove them in order to get the scatter sinograms. These are then smoothed and subtracted from the data recorded in the regular window [Bendriem et al., 1994, Zaidi and Koral, 2006]. For more information regarding this method, please refer to the original article published by Bendriem et al. [1994].

2.6.4.2 Single Scatter Simulation (SSS)

The Single Scatter Simulation (SSS) is a model-based algorithm which provides a good scatter estimate within reasonable computational time. This means that the SSS uses a physical model of the medium in order to estimate the scatter distribution. The steps of the algorithm can be summarised as follows [Accorsi et al., 2004]:

1. Use emission image to define emission distribution and attenuation map to define attenuation distribution.
2. Distribute the scatter points randomly within the scatter volume.
3. Choose a LOR. Considering the case in figure 2.13, the LOR would be \overline{AB} .
4. For a given scatter point S (figure 2.13), calculate the number of events that contribute to \overline{AB} . This calculation takes into account the activity distribution along \overline{SA} and \overline{SB} , and the probability of a photon being scattered in the direction of B (if it is originated somewhere along \overline{AS} and suffers a Compton scatter in S) or A (if it is originated somewhere along \overline{BS} and suffers a Compton scatter in S).

This calculation takes into account the distribution of the activity, scatter medium distribution, solid angles, Compton scatter relationships and the Klein-Nishina cross-section [Accorsi et al., 2004].

In this case, the contribution of the scatter point S to \overline{AB} is given by:

$$I_{A,S,B} = I_A + I_B \quad (2.19)$$

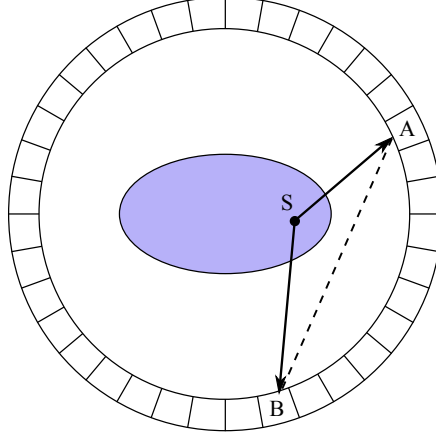


Figure 2.13: Selection of a scatter point (S) and a LOR (\overline{AB}) in the SSS algorithm.

where

$$I_A \propto \int_A^S f(\xi) d\xi \exp\left(-\int_A^S \mu(E_0, \xi) d\xi\right) \exp\left(-\int_B^S \mu(E_s, \xi) d\xi\right) \varepsilon_A \varepsilon_B \frac{\mu_C(E_0, S)}{\sigma} \frac{d\sigma}{d\Omega} \Omega_B \quad (2.20)$$

and

$$I_B \propto \int_B^S f(\xi) d\xi \exp\left(-\int_B^S \mu(E_0, \xi) d\xi\right) \exp\left(-\int_A^S \mu(E_s, \xi) d\xi\right) \varepsilon_A \varepsilon_B \frac{\mu_C(E_0, S)}{\sigma} \frac{d\sigma}{d\Omega} \Omega_A \quad (2.21)$$

The activity distribution is represented by $f(\xi)$, where ξ is an integration variable spanning the line between the limits. The variables E_0 and E_s are the energies of the photon before and after the Compton interaction (section 2.2.2.2), respectively. $\mu(E, \xi)$ is the attenuation coefficient for all the types of interactions that remove the photon from the straight line (dependent on the energy and position) and $\mu_C(E_0, \xi)$ is the attenuation coefficient only for Compton scattering (dependent on the energy and position). $\frac{d\sigma}{d\Omega}$ is the Klein-Nishina differential cross-section and σ is the Klein-Nishina total cross-section. Ω_A and Ω_B correspond to the solid angle under which detectors A and B are seen from S , respectively. Finally, ε_A and ε_B are factors related to the detection efficiencies of detectors A and B , respectively. For more information regarding these factors, please refer to the article published by Accorsi et al. [2004].

5. Select another S and repeat step 4.
6. Select another LOR and repeat the two previous steps.
7. Make interpolations in the LOR space in order to obtain the scatter sino-

grams.

8. The simulated scatter sinograms are not properly scaled to the measured data, i.e. only the overall distribution is estimated rather than absolute values. Thus, the obtained values of the SSS have to be scaled using the scatter tails as reference. The choice of the tails as the reference is due to the fact that they are scatter-only regions. Thus, if the scaling is performed correctly in this region, it is assumed that the rest will be properly scaled.
9. The prompt data are corrected and reconstructed. One of the most straightforward ways to correct for the scatter is to subtract the scaled scatter sinograms from the prompts sinograms. However, it is not the only option.

One of the problems of this algorithm is that it estimates the scatter using an emission image that was reconstructed from data that is already biased due to Compton scattering. This can be corrected by iterating the SSS, reusing the emission data from previous iterations [Werling et al., 2002]. Another major concern with this algorithm is the fact that it only takes into account single scattered events. In a real data acquisition, there are events in which both photons are scattered, in addition, any photon can be scattered multiple times before reaching the detector. These are known as *multiple scattered events*.

This effect is more prominent in larger objects. The distribution of the multiple scattered events is usually broader than the distribution of single scattered events. Thus, SSS is only an approximation of the true scatter distribution [Accorsi et al., 2004].

An image corrected for randoms, attenuation and scatter is shown on the left side of figure 2.14. By comparing this image to the previous uncorrected ones (figures 2.11 and 2.12), one can see that the scatter tails have been removed and the intensity distribution inside the cylinder is uniform.

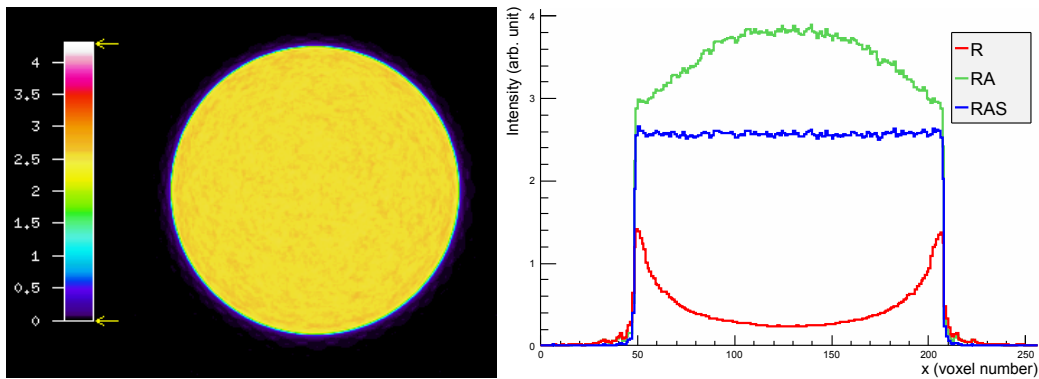


Figure 2.14: Left - Simulated uniform cylinder with scatter correction. The image was corrected for random events (R), attenuation (A), Compton scattering (S) and reconstructed using OP-OSEM with 8 iterations and 2 subsets; Right - Intensity profile of figure 2.11 (R profile, red), figure 2.12 (RA profile, green) and the profile of the cylinder after applying all the corrections (RAS profile, blue); the simulated data were generated following the procedure described in section 3.7.

2.7 Image Reconstruction

This section will describe the most common reconstruction algorithms. These will be divided into Backprojection Techniques (section 2.7.1) and Iterative Reconstruction Algorithms (section 2.7.2).

2.7.1 Backprojection Techniques

2.7.1.1 Simple Backprojection

The objective of a reconstruction method is to use the information in the measured projection data to obtain the image of the activity distribution within the object $f(x, y)$. One of the simplest methods for image reconstruction in PET is the *backprojection*.

The information saved in the sinogram can be understood as a set of projection profiles $p(r, \phi_i)$ acquired at discrete angles ϕ_i and with each projection sampled at discrete intervals along the radial coordinate r [Cherry et al., 2003].

Using backprojection, the profile acquired at each angle will be projected back into the image space, which means that the number of counts acquired at each projection line will be uniformly distributed between the pixels along that path (figure 2.15) [Cherry et al., 2003].

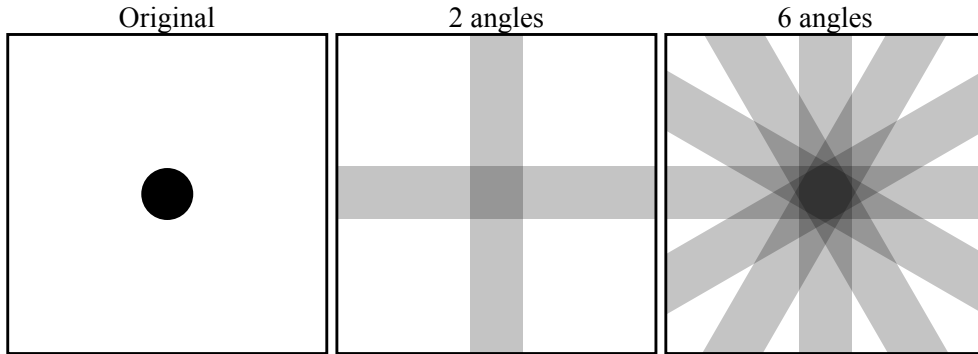


Figure 2.15: Representation of a cylinder phantom (left); Representation of the acquired images using backprojection with two angles (centre) and six angles (right). The images are only illustrations to explain the concept.

By taking into account the following equation:

$$r = x \cos \phi + y \sin \phi \quad (2.22)$$

the value of each voxel in the resulting image can be defined as:

$$f'(x, y) = \frac{1}{N} \sum_{i=1}^N p(x \cos \phi_i + y \sin \phi_i, \phi_i) \quad (2.23)$$

where $f'(x, y)$ is the approximation to the true distribution $f(x, y)$, N is the number of profiles and ϕ_i is the i^{th} projection angle [Cherry et al., 2003].

One of the disadvantages of this technique can be clearly seen in figure 2.15, where blurring will occur due to the projection of information outside the true location of the object. The quality of the image can be improved by using more projections. However, blurring will always occur, even with an infinite number of projections [Cherry et al., 2003].

2.7.1.2 Filtered Backprojection

Before explaining how the filtered backprojection (FBP) method works, one needs to introduce some concepts about *Fourier transforms* (FTs).

FT allows the representation of a spatially varying function $f(x)$ in image space as a sum of sine and cosine functions of different spatial frequencies k in “spatial frequency space”, also known as k -space [Cherry et al., 2003]. The operation is represented as:

$$F(k) = \mathcal{F}[f(x)] \quad (2.24)$$

The original $f(x)$ function can be recovered by applying the *inverse FT*, which is represented as:

$$\mathcal{F}^{-1}[F(k)] = f(x) \quad (2.25)$$

These concepts about FT in one dimension can be applied to two dimensional spaces, like the projection space $p(r, \phi)$, by using the *projection slice theorem*, which states:

$$\mathcal{F}[p(r, \phi)] = P(k_r, \phi) \quad (2.26)$$

where $P(k_r, \phi)$ is the value of the FT at a radial distance k_r along a line at angle ϕ in k -space [Cherry et al., 2003].

In order to use these concepts to reconstruct an image, one must first measure the projection profiles $p(r, \phi)$ at the N projection angles and apply the FT to each projection profile (equation 2.26). Then, a *ramp filter* is applied to the resulting $P(k_r, \phi)$, which essentially means that each projection is multiplied by $|k_r|$ [Cherry et al., 2003]:

$$P'(k_r, \phi) = |k_r|P(k_r, \phi) \quad (2.27)$$

After the ramp filter is applied, the inverse FT for each projection profile is calculated:

$$p'(r, \phi) = \mathcal{F}^{-1}[P'(k_r, \phi)] = \mathcal{F}^{-1}[|k_r|P(k_r, \phi)] \quad (2.28)$$

Finally, the image can be reconstructed using the filtered projection $p'(r, \phi)$ and equation 2.23:

$$f(x, y) = \frac{1}{N} \sum_{i=1}^N p'(x \cos \phi_i + y \sin \phi_i, \phi_i) \quad (2.29)$$

where $f(x, y)$ is the discretized true distribution. Unlike in the case of a simple backprojection, the FBP allows one to reconstruct the exact discretized true distribution. However, this is only in theory, since measured data contains noise,

which will degrade image quality [Cherry et al., 2003].

Due to its speed and relative ease of implementation, the FBP is one of the most popular reconstruction methods. However, it presents some limitations, such as:

- Data sets with low counting statistics produce streak artefacts [Cherry et al., 2003];
- The FBP method cannot be modified to take into account various characteristics of the PET system, such as: the limited spatial resolution of the detectors, scattered events, etc. These require extra processing [Cherry et al., 2003].

2.7.2 Iterative Reconstruction Algorithms

These algorithms are computationally more intensive than FBP. However, due to the improvements in processing speed, they are currently used routinely in PET reconstruction. The general concept is illustrated in figure 2.16.

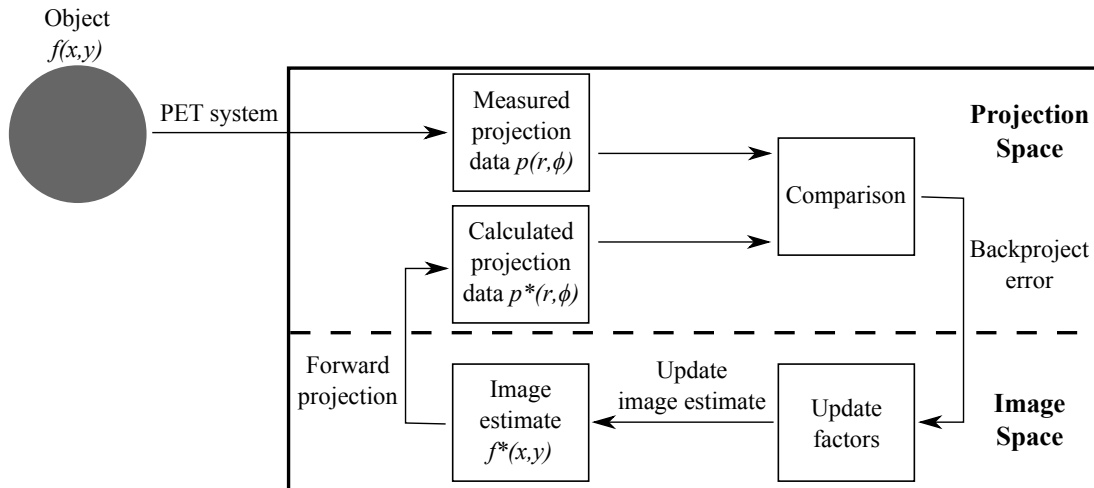


Figure 2.16: General concept of the iterative reconstruction algorithms.

The algorithm approaches the true distribution $f(x, y)$ through a succession of estimates $f^*(x, y)$. The first estimation is usually very simple (a uniform or a blank image). Then, this image is submitted to a process called *forward projection*, which generates a detector response from the current image. This process involves the sum of all the intensities along the ray paths for all LORs [Cherry et al., 2003].

The calculated projection data $p^*(r, \phi)$ is compared with the measured data $p(r, \phi)$. The error in projection space is then backprojected into image space and used to update $f^*(x, y)$. This procedure is iteratively repeated to successively improve the image estimate.

By taking into account how the iterative reconstruction algorithms work, one can understand why are these slower than the FBP. One reason lies with the fact

that most of them need several iterations in order to converge to an acceptable result. Each iteration includes a forward projection and backprojection, each one taking approximately the same amount of time. The backprojection is the most time consuming step in a FBP, which explains why repeating it several times makes the iterative reconstruction algorithms slower than the FBP [Cherry et al., 2003].

The iterative algorithms have two main components: the method to compare $p(x, y)$ and $p^*(x, y)$, and the method to update $f^*(x, y)$ in each iteration. The former is performed by the *cost function* and the latter by the *update function*. Iterative algorithm development is essentially focused in the use of new functions to perform each one of these steps [Cherry et al., 2003].

Two iterative algorithms are presented in the following sections: the *Maximum Likelihood Expectation Maximization* (MLEM) and the *Ordered Subsets Expectation Maximization* (OSEM).

2.7.2.1 Maximum Likelihood Expectation Maximization (MLEM)

The MLEM algorithm estimates the most likely source distribution by taking into account statistical considerations [Cherry et al., 2003, Matela, 2008].

The acquired data will be represented by vector \mathbf{p} , where p_j is the number of counts in the j^{th} projection element. This measured data can be related to the activity in each voxel by:

$$p_j = \sum_i M_{i,j} f_i \quad (2.30)$$

where f_i is the number of photon pairs emitted in voxel i and $M_{i,j}$ is the system matrix, which gives the probability that the photon pair emitted in the i^{th} voxel is detected in the j^{th} projection element [Matela, 2008].

With equation 2.30 in mind and by taking into account its statistical nature (Poisson statistics) and the maximum likelihood, the following formula is deduced:

$$f_i^{k+1} = \frac{f_i^k}{\sum_j M_{i,j}} \times \sum_j M_{i,j} \frac{p_j}{\sum_v M_{v,j} f_v^k} \quad (2.31)$$

where k is the iteration number. Thus, f_i^{k+1} is the activity associated with pixel i in the next iteration.

The elements in equation 2.31 can be related to the scheme in figure 2.16. The sum $\sum_v M_{v,j} f_v^k$ corresponds to the forward projection step, in which the information in image space is converted to projection space (equation 2.30). The measured data p_j is then compared with the estimated data by calculating the ratio. The ratio is weighted by the system matrix element $M_{i,j}$ and summed, which gives the update factor for each voxel i . Finally, by multiplying the update factors with the current estimation (divided by the sensitivity in image space $\sum_j M_{i,j}$), the image is updated [Matela, 2008].

The MLEM algorithm provides a good estimation of the real distribution. However, it suffers from two major problems: the speed (which is lower when

compared with FBP) and the stability.

The algorithm tries to find the intensity distribution that best fits the measured data. However, the data contains noise, which means that the algorithm will converge to a noisy solution. One way to avoid this is by stopping the algorithm before the image becomes too noisy. However, this results in an image with reduced resolution (i.e. a smoother image) [Matela, 2008].

For more information regarding the deduction of equation 2.31, please refer to the thesis by Matela [2008].

2.7.2.2 Ordered Subsets Expectation Maximization (OSEM)

The Ordered Subsets Expectation Maximization (OSEM) algorithm was proposed by Hudson and Larkin in 1994 [Hudson and Larkin, 1994]. It is similar to the MLEM algorithm, but the projection data is divided into subsets, in order to reduce the computational time. Equation 2.31 can be rewritten to express this method:

$$f_i^{k+1} = \frac{f_i^k}{\sum_{j \in S_n} M_{i,j}} \times \sum_{j \in S_n} M_{i,j} \frac{p_j}{\sum_v M_{v,j} f_v^k} \quad (2.32)$$

where S_n is the n^{th} subset.

One can see the similarities between equation 2.32 and equation 2.31. However, this time the sum of the projection data is not performed to the data as a whole. Instead, subset iterations are performed only to the projections belonging to each subset S_n .

This algorithm is faster than the MLEM. However, it presents even more problems regarding the stability.

Materials and Methods

In this chapter, different materials and methods used in this thesis shall be described.

This chapter will start by describing the BrainPET scanner installed at the Forschungszentrum Jülich and the organization of the acquired data (section 3.1).

Then, the method used for identifying the scatter tails will be explained (section 3.2). This is especially important to select the data that are used by the scatter scaling methods, which will be explained in sections 3.3, 3.4 and 3.5.

An alternative method for selecting the data to be used by the scatter scaling methods will be described in section 3.6.

The methods used to generate simulated data and to acquire real data will be described in sections 3.7 and 3.8, respectively.

Finally, the performed tests will be explained in section 3.9.

3.1 BrainPET Scanner

3.1.1 Hardware

The BrainPET scanner is a MR-compatible PET system designed by Siemens for human brain studies. It was installed at the Forschungszentrum Jülich in 2008 and it consists in a PET system that can be inserted into the bore of a 3T Magnetom TRIO MR scanner, allowing the simultaneous acquisition of PET and MR data [Schlemmer et al., 2008].

The system is composed of 32 detector cassettes, each one shielded with copper. The cassettes form a ring with a 60 cm outer diameter, 36 cm inner diameter and with a length of 72 cm (figure 3.1). This allows for a Field-Of-View (FOV) of 19.2 cm in the axial direction and a transaxial FOV with a diameter of 36 cm [Schlemmer et al., 2008].

A detector cassette contains 6 detector blocks. Each block consists of a 12×12 array of LSO crystals, coupled to a 3×3 array of APDs, being the size of the

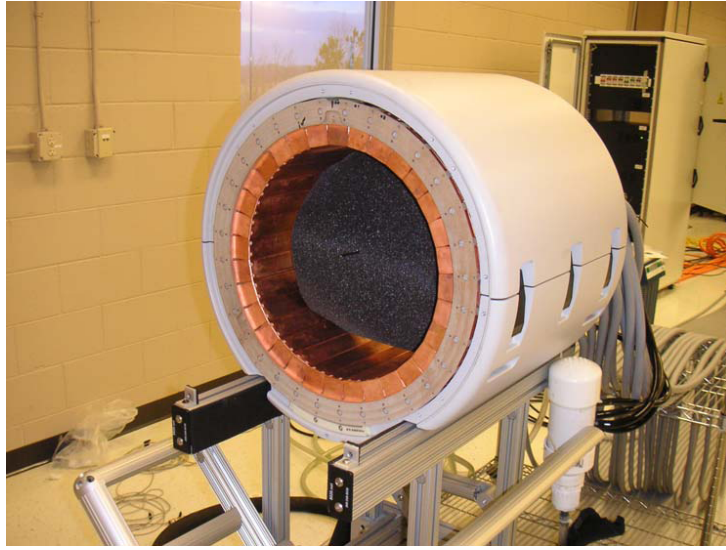


Figure 3.1: The BrainPET scanner at the Forschungszentrum Jülich.

individual LSO crystals $2.5 \times 2.5 \times 20$ mm [Schlemmer et al., 2008]. The detectors are separated by gaps, which will result in some diagonal stripes in the acquired sinograms (section 3.2)

The BrainPET system has a timing window of 12 ns for coincidence measurement.

3.1.2 Organization of the Sinogram Files

Understanding how the sinogram files from the BrainPET scanner are organized is essential to manipulate the projection data. Each sinogram file is composed of 1399 *sinogram planes* (from plane 0 to plane 1398), i.e. 1399 different sinograms. The distribution of the sinogram planes between the different segments is illustrated in table 3.1.

Each sinogram is composed of 192 bins in the angular coordinate (192 views covering 180°), and 256 bins in the radial direction with a radial resolution of 0.125 cm (which equals a total of 32 cm). This results in 49 152 bins per plane and 68 763 648 bins per sinogram file.

Table 3.1: Organisation of the segments in a BrainPET sinogram file.

Segment	Start Plane	End Plane
0	0	152
-1	153	295
1	296	438
-2	439	563
2	564	688
-3	689	795
3	796	902
-4	903	991
4	992	1080
-5	1081	1151
5	1152	1222
-6	1223	1275
6	1276	1328
-7	1329	1363
7	1364	1398

3.2 Classification of the Scatter Tails

The SSS algorithm provides an estimation of the scatter distribution, but this is not scaled (section 2.6.4.2). Since the measured tails contain only random and scattered counts, these are used as reference values for the scaling. If one can adequately scale these scatter tails, the rest of the distribution is assumed to be scaled properly and the image can be corrected for scatter.

In order to classify the tails, the regions outside the object must be identified. To do this, the attenuation map of the object was forward projected and the ACFs were determined in projection space. The obtained ACFs are used to identify the regions outside the object. Equation 2.18 shows that if the medium is composed of air ($\mu_{\text{air}} \approx 0 \text{ cm}^{-1}$), then, $I_0/I = 1$ (i.e. $\text{ACF} = 1$).

Several tests in this thesis were performed with simulated data, in which a mathematical cylinder phantom was used to generate the attenuation sinograms (section 3.7). The first step was to generate a 10 cm radius cylinder image with a length equal to the length of the FOV and with an attenuation coefficient equal to the one of water for 511 keV photons (0.096 cm^{-1}). This was then forward projected (figure 3.2), which means that the ACF values (equation 2.18) will be represented in several sinograms.

In figure 3.2, the regions outside the phantom correspond to the bins with a value equal to 1. A mask can be generated which contains only these regions. This was done by setting all the values greater than 1 to 0. However, this mask does not yet consider the gaps caused by the gaps between the detectors of the PET scanner (section 3.1.1). The gaps can be extracted from the normalisation sinogram file (figure 3.3).

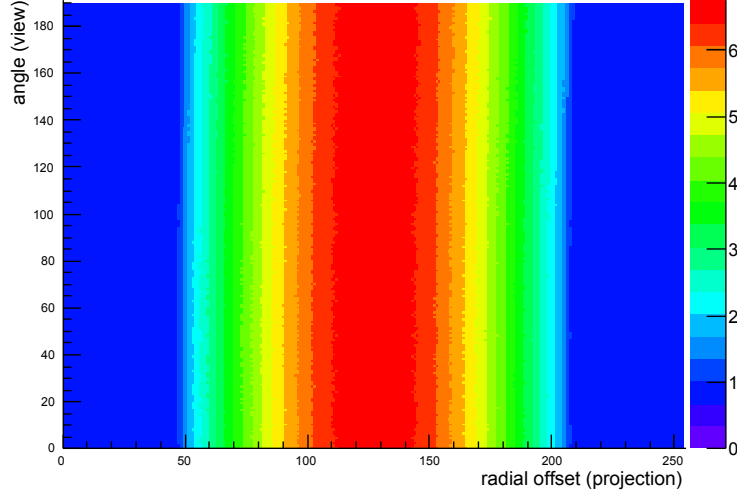


Figure 3.2: Generated attenuation sinogram file from a 10 cm radius cylinder phantom (plane 1). The region outside the phantom is represented in dark blue ($ACF = 1$).

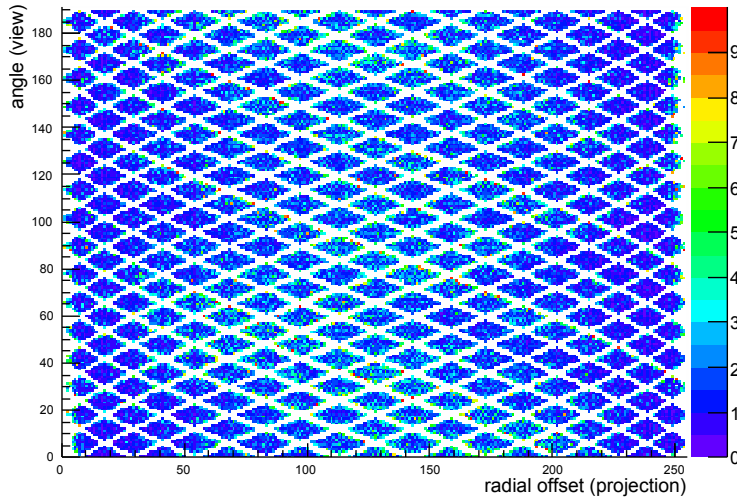


Figure 3.3: Normalisation sinogram file (plane 1). The diagonal white stripes are caused by the gaps between the detectors.

In order to include the gaps and to mask other bins which do not contribute with any counts, the normalisation sinograms can also be used to generate a mask. In this case, all bins with values greater than 0 are set to 1. Finally, this mask can be multiplied by the mask generated from the attenuation sinograms in order to obtain the final tail mask (figure 3.4). This can be used by the scatter scaling methods to identify all bins which should be used for scaling.

The process used to generate the tail mask is summarized in figure 3.5.

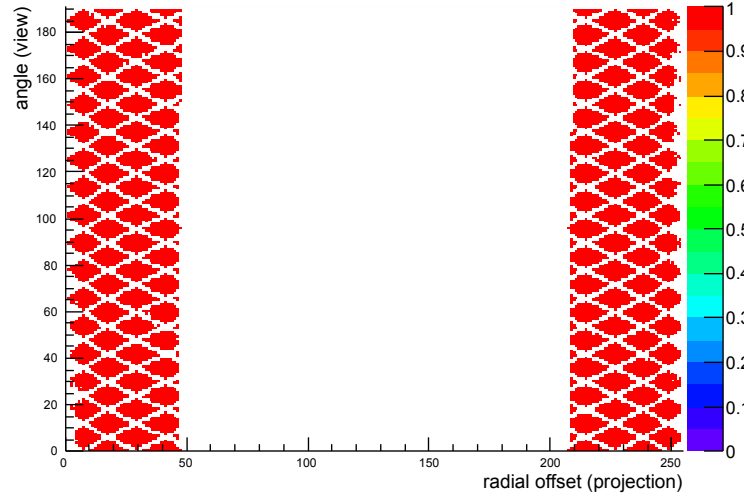


Figure 3.4: Tail mask (plane 1).

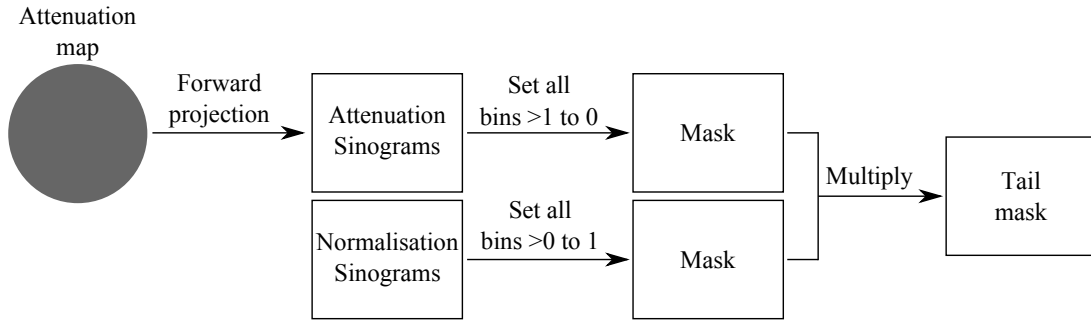


Figure 3.5: Process used to generate the tail mask.

3.3 Standard Scaling Method

The scaling method used in the software packages provided by Siemens is divided into two steps. The first consists in determining the scaling factor for each sinogram plane individually, then, the results are filtered using a boxcar filter.

The scaling factor for each plane p is calculated using the following equation:

$$\alpha_p = \frac{\sum_i N_{i,p}(P_{i,p} - R_{i,p})S_{i,p}}{\sum_i S_{i,p}^2} \quad (3.1)$$

where α_p is the scaling factor for plane p , $N_{i,p}$ is the value of bin i (of plane p) of the normalisation sinogram file, $P_{i,p}$, $R_{i,p}$ and $S_{i,p}$ correspond to the values of the corresponding bins in the prompt, random and scatter sinogram files, respectively. Note that only the bins corresponding to the tails are used for the evaluation (section 3.2).

In the standard procedure the applied boxcar filter has a 7 plane margin, which means that for a given plane p , its α_p value will be:

$$\alpha_p = \frac{1}{N} \sum_{j=(p-7)}^{p+7} \alpha_j \quad (3.2)$$

where N is the number of planes used, which can be lower than 15 if plane p is close to one of the limits of the corresponding segment (table 3.1), i.e. the planes used by the boxcar filter must belong to the same segment. This filter will ensure that the variation of the scaling factors with the plane number is smooth.

3.4 Non Pre-Corrected Data (NPCD) Scaling Method

In the standard scaling method, the data are pre-corrected by being subtracted by expected randoms and multiplied by $N_{i,p}$ (equation 3.1). This can affect the results due to the statistical uncertainties and error propagation.

The equation can be slightly modified in order to estimate the scaling factor without pre-correcting the data. This is achieved by dividing the scatter data (which is already normalised) by the normalisation data, thus, cancelling the normalisation and estimating the scaling factor with *Non Pre-Corrected Data* (NPCD). The equation of the new scaling method can be written as:

$$\alpha_p = \frac{\sum_i (P_{i,p} - R_{i,p}) \frac{S_{i,p}}{N_{i,p}}}{\sum_i \left(\frac{S_{i,p}}{N_{i,p}} \right)^2} \quad (3.3)$$

Despite the similarities between equations 3.3 and 3.1, they are not equivalent. In equation 3.3, the values of the scatter sinogram file ($S_{i,p}$) are modified instead of the values of the prompts sinogram file ($P_{i,p}$). Unlike the prompts sinograms, the scatter sinograms do not have statistical uncertainties. Thus, error propagation does not enhance the errors of the values in the scatter sinograms.

Just as in the case of the Standard scaling method (section 3.3), a boxcar filter can then be applied to smooth the variation of the scaling factors with the plane number.

3.5 Maximum Likelihood (ML) Scaling Method

The previous scaling methods provide a simple and straightforward way of estimating the scaling factors. However, they do not directly account for Poisson noise (section 2.3). Therefore, another method is proposed in which this factor is accounted for. This approach should improve the scaling factor estimation.

According to equation 2.10, one can determine the probability of measuring $P_{i,p}$ as:

$$P(P_{i,p}|\lambda_{i,p}) = \frac{\lambda_{i,p}^{P_{i,p}} e^{-\lambda_{i,p}}}{P_{i,p}!} \quad (3.4)$$

where the expectation value $\lambda_{i,p}$ is defined as: $\lambda_{i,p} = R_{i,p} + \alpha_p \frac{S_{i,p}}{N_{i,p}}$.

The probability of bin i in plane p to observe a certain value $P_{i,p}$ can be calculated using equation 3.4. This probability explicitly depends on the value of the scaling factor α_p . By multiplying the probabilities for all the bins, the likelihood of a certain α_p being the optimal scaling factor for plane p is obtained. This can be written as:

$$\mathcal{L}_p = \prod_{i=0}^N \frac{\left(R_{i,p} + \alpha_p \frac{S_{i,p}}{N_{i,p}}\right)^{P_{i,p}}}{P_{i,p}!} e^{-\left(R_{i,p} + \alpha_p \frac{S_{i,p}}{N_{i,p}}\right)} \quad (3.5)$$

Equation 3.5 can be simplified as:

$$\ln(\mathcal{L}_p) = \sum_{i=0}^N P_{i,p} \ln \left(R_{i,p} + \alpha_p \frac{S_{i,p}}{N_{i,p}} \right) - \ln(P_{i,p}!) - \left(R_{i,p} + \alpha_p \frac{S_{i,p}}{N_{i,p}} \right) \quad (3.6)$$

The goal of the *Maximum Likelihood* (ML) scaling method is to find the maximum of equation 3.6 as a function of the scaling factor, thus giving the most likely scaling factor. Since the absolute value of $\ln(\mathcal{L}_p)$ is not relevant to find the maximum, the equation was further simplified in order to reduce the computational time (equation 3.7).

$$\ln(\mathcal{L}_p) = \sum_{i=0}^N P_{i,p} \ln \left(R_{i,p} + \alpha_p \frac{S_{i,p}}{N_{i,p}} \right) - \left(R_{i,p} + \alpha_p \frac{S_{i,p}}{N_{i,p}} \right) \quad (3.7)$$

In the region where $\alpha_p \geq 0$, the function defined by equation 3.7 has one clearly defined maximum close to the scaling factor as estimated by equations 3.1 and 3.3 (figure 3.6). This makes it easy to find and to fix the optimal scaling factor.

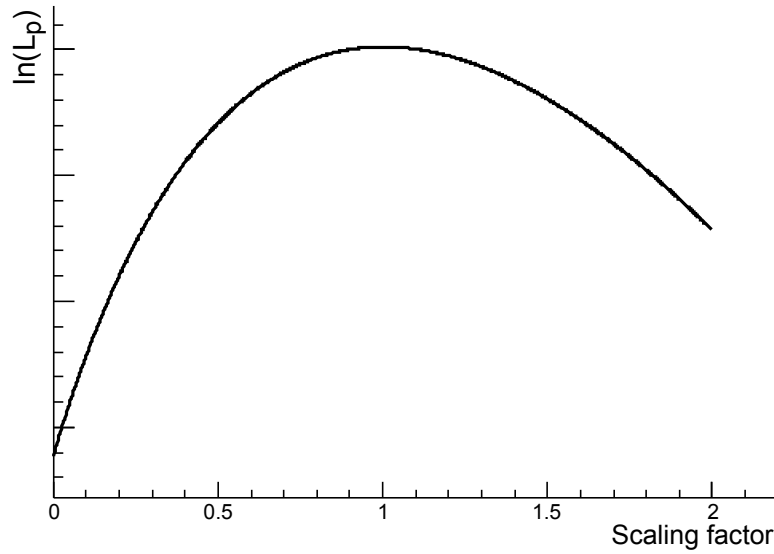


Figure 3.6: Plot of the function defined in equation 3.7. In this case, the theoretical scaling factor is 1. The object used for acquiring the data was a uniform cylinder. It was simulated using the method described in section 3.7 with 1×10^{10} true counts and $p = 36$.

3.6 Plane Integration

Sometimes the amount of data available in one sinogram plane is not sufficient to make an accurate estimation of the scaling factor. This is particularly true in the case of short time frames, due to the low number of counts. The proposed solution consists in adding the data from adjacent planes, thus, “integrating” the planes and increasing the amount of data available.

In a 3D-PET measurement, several segments corresponding to different detector ring combinations are acquired. When performing a Plane Integration (PI), one has to bear in mind that all the planes integrated must belong to the same segment. Thus, the PI must be confined to the plane intervals defined in table 3.1.

In the case that the plane for which the scaling factor is being estimated is close to the start or end planes, it can happen that the distribution of planes integrated is becoming asymmetric. For example, if the scaling factor estimation for plane 100 is done with the integration of 3 planes (i.e. a 1 plane margin), then, planes 99, 100 and 101 will be used. However, when the same PI is applied to plane 152, then, only planes 151 and 152 will be used (2 out of 3), since plane 153 belongs to another segment (table 3.1). This means that the scaling factor estimation for these planes will use less statistics. The boxcar filter uses an analogous procedure: it only averages the scaling factors that are within the plane margin and belong to the same segment (equation 3.2).

The amount of planes to be integrated must be chosen carefully. If a plane p is adjacent to other planes which have a very different scatter contribution, the integration of counts from these planes will have a negative effect on the

estimation of the scaling factor α_p . Therefore, the data used in this thesis were always from uniform cylinder phantoms (sections 3.7 and 3.8). This will ensure that the scatter contribution from all the planes is more uniform.

3.7 Generation of Simulated Data

The use of simulated data to test the scaling methods is very advantageous because one knows the correct result beforehand, i.e. the correct scaling factor. Therefore, the three methods can be compared on how accurately they estimate the scaling factor.

Five samples of different statistics have been used for this work, each one consisting of three simulated sinogram data sets: one containing the true counts, another containing random counts and one containing scattered counts. The first was generated by forward projecting a 20 cm diameter uniform cylinder phantom without calculating the ACFs. The random data were extracted from a real measurement of a ^{18}F filled cylinder with the same dimensions, this was the only data set that was originated from real data. The scattering data were the result of a scatter estimation using the uniform cylinder phantom as emission image and a uniform cylinder phantom with the attenuation coefficient of water (0.096 cm^{-1}) as the attenuation map. The attenuation sinograms (containing the ACFs) were generated by forward projecting the attenuation map.

The attenuation and detector sensitivity were taken into account for the sinograms with the true counts by dividing them by the attenuation sinograms and a normalisation sinograms previously estimated in the BrainPET. The random fraction and the scatter fraction were adjusted to be 20% and 30%, respectively. These fractions were chosen for being relatively common in PET [Valk et al., 2003].

The total number of true counts of the samples were: 1×10^6 , 1×10^7 , 1×10^8 , 1×10^9 and 1×10^{10} . These values were chosen to cover a wide range of statistical levels that can be acquired with PET.

Using the three contributions of each sample, noisy prompts sinograms were generated. In order to do so, the scatter sinograms were first divided by the normalisation sinograms, to account for the detector sensitivity. Then, the trues sinograms (T), randoms sinograms (R) and scatter sinograms (S) were added and Poisson noise was introduced, generating the prompts sinograms:

$$P_{\text{noise}} = (T + R + S)_{\text{noise}} \quad (3.8)$$

The original non-noisy version of the scatter sinograms (S) was used as the unscaled scatter distribution when testing the scatter scaling algorithms (section 3.9.1). Thus, the correct scaling factor should be 1 for all sinogram planes, since the scatter distribution in the noisy prompts data is a noisy version of the one that is being used for estimating the scaling factor.

3.8 Acquisition of Real Data

A measurement was performed in the BrainPET scanner in which a 20 cm diameter and 20 cm length cylinder phantom was filled with water containing ^{18}F (figure 3.7).



Figure 3.7: 20 cm diameter and 20 cm length cylinder phantom used for the acquisition of real data.

The initial activity of the cylinder was 226 MBq and the data was acquired for 10 half-lives. Since the half-life of the tracer is 6586 s, the measurement lasted more than 18 h. However, the data range used for this study was only from 10 s to 6400 s.

The test performed with these data will be explained in section 3.9.2.

3.9 Evaluation of Performance

The scatter scaling methods were tested both with simulated data and real data. However, the tests performed with each type of data were different. These will be explained in the following sections.

3.9.1 Simulated Data

3.9.1.1 Comparison of the Scaling Methods

The three scaling methods described in sections 3.3, 3.4 and 3.5 were tested using only plane 36 of the sinogram files. This was done to evaluate how each method performs in the estimation of the scaling factor α_p for a single plane p .

The scaling factor estimation was done without a boxcar filter or PI. Plane 36 was chosen because it is located in the middle of the segment 0, thus avoiding any unwanted effects that might occur at the end of the segments.

The test started by taking the sinograms from one of the samples (e.g. 1×10^6) and to generate the prompts sinograms (section 3.7). Then, each one of the scaling methods was applied and the corresponding scaling factors were stored. The process was repeated 300 000 times for all the samples in order to acquire a statistically significant sample size within a reasonable computational time.

After all the scaling factors were obtained, their distribution was plotted for the individual scaling methods at different levels of statistics and for all the scaling methods at the same level of statistics. The results were then compared (section 4.1.1).

3.9.1.2 Plane Integration *versus* Boxcar Filter

The purpose of this test was to compare the distributions of the scaling factors by using the different scaling methods with a boxcar filter or PI. This was done to determine if the use of PI improves the estimation of the scaling factors when compared with the currently used boxcar filter.

The procedure was similar to the one in section 3.9.1.1, in which the three methods were used to calculate the scaling factor of plane 36 multiple times. However, this time the process was also repeated using a boxcar filter and PI with 8 different plane margins, from 0 (single plane) to 7. Since plane 36 is in the middle of the segment (table 3.1), the planes used for the PI and the boxcar filter have a symmetric distribution (section 3.6).

This test required much more computational time than the one in section 3.9.1.1. Therefore, the number of repetitions was reduced.

There were 5 samples with different levels of statistics. For each one, the three scaling methods were tested both using a boxcar filter and PI with 8 different plane margins. This means that 240 distributions were obtained. Repeating the process 300 000 times for each distribution would be very time-consuming. Also, the use of PI makes the process more time-consuming, since the amount of data used to estimate each scaling factor is greater. Thus, only 10 000 scaling factors were obtained for each distribution.

The results of this test will be presented in section 4.1.2.

3.9.1.3 Evaluation of Error Sources

There are several error sources in scatter correction. In order to test the influence of each one, several tests were performed in which errors were deliberately introduced in the data and the images reconstructed. These were then compared with the normal images.

The methods used to test each error source are described below.

Error in the scatter scaling factor

The first error source tested was the incorrect scaling of the scatter. In order to have an idea of its effect, the image of the uniform cylinder phantom with 1×10^8 true counts was reconstructed with the scatter properly scaled ($\alpha_p = 1.0$),

underestimated by 10% ($\alpha_p = 0.9$) and overestimated by 10% ($\alpha_p = 1.1$). The images were reconstructed using OP-OSEM with 8 iterations and 2 subsets and compared (section 4.1.3.1).

Error in the random estimation

When the estimated scatter tails are scaled to the measured tails, the latter ones have to be corrected for random counts. This can be seen in equations 3.1 and 3.3, where the randoms are subtracted from the prompts. Equation 3.7 takes a different approach, but the randoms are also present.

In the tails, the amount of scattered counts is very low. Therefore, if the amount of random counts is similar to the scattered counts, a small error in the estimation of the randoms can have a noticeable effect on the scaling of the scatter tails.

To test the influence of small variations in the estimated randoms, two randoms sinogram files were generated. These consisted in the original sinogram files scaled down by 10% and scaled up by 10%. Then, these sinograms were used to calculate the scaling of the scatter and to reconstruct the images. The resulting images were then compared with the image reconstructed with the correct nominal setup (section 4.1.3.2).

Use of the image corrected for random counts and attenuation to estimate the scatter

So far, the scatter estimation was performed using the emission phantom as the emission image. However, in a PET data acquisition, no such image is available. Therefore, the normalised emission image corrected for the attenuation effect and the random counts is used as emission image. This image shall be referred to as the *RA image* and the scatter corrected image as the *RAS image*.

The results acquired using the RA image over the phantom image to estimate the scatter distribution were worse due to the bias in the RA image. Thus, some tests were performed to determine if they can be improved.

One of the tests consisted in repeating the scatter estimation using the RAS image and use the new scatter sinogram file to reconstruct a new RAS image. The process is represented in figure 3.8.

As one can see in figure 3.8, the RA image and attenuation map were used to perform the first scatter estimation. This was used to correct the prompts sinograms and reconstruct the first RAS image, which shall be referred to as RAS_00. To correct the bias in the RAS_00 image, this was used as emission image in a new scatter estimation. The reconstruction with the new scatter estimation resulted in another RAS image (RAS_01). The process was repeated 10 times, resulting in 11 RAS images (from RAS_00 to RAS_10). These were compared with a reference image reconstructed using the sinograms containing only the true counts.

Two more images were tested. One had the same distribution of the true counts as the original phantom image, but the amount of scatter in the data was

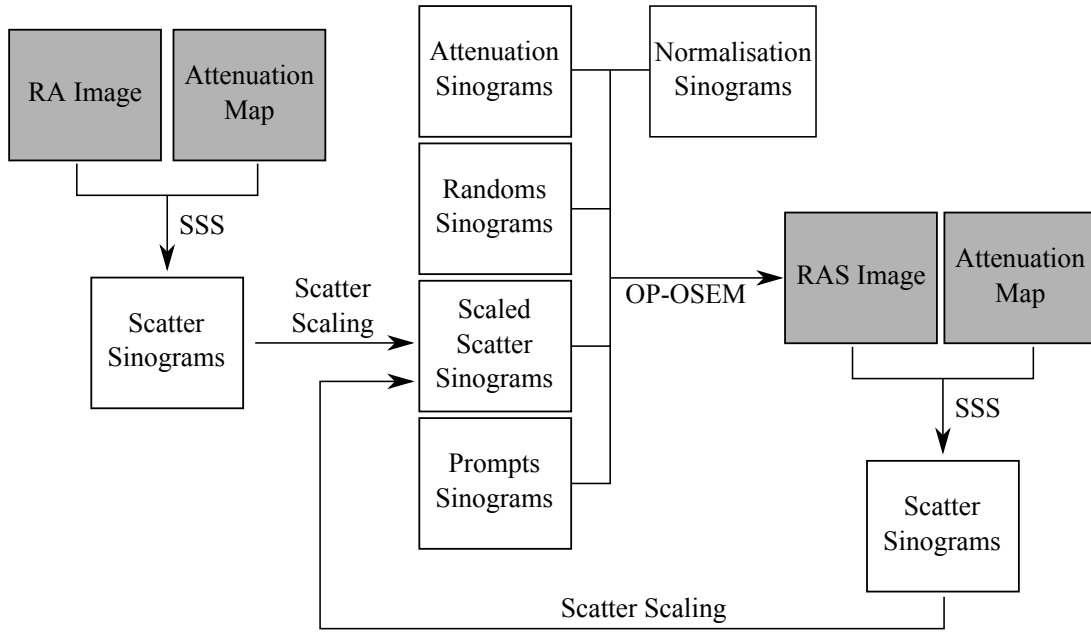


Figure 3.8: Scheme of the approach taken to try to correct for Compton scattering without using the phantom image.

increased from 30% to 50%. As explained in section 2.5.2, these are common scatter fractions in 3D-PET acquisitions. This was done to see if the approach explained in figure 3.8 works with data containing a higher scatter fraction.

The other image had the scatter fraction as the first image (30%) but the intensity distribution was not uniform. In this case, the intensity distribution in the cylinder phantom was as follows:

$$I(x, y) = \begin{cases} 0.5 & \text{if } r \leq 2.5 \\ 1 & \text{if } 2.5 < r \leq 10 \end{cases} \quad (3.9)$$

where $I(x, y)$ is the image intensity in a certain voxel and r is the distance of that voxel to the central axis of the cylinder [cm]. The attenuation map used for this image was the same as the previous ones. Also, the number of true counts was increased to 1×10^{10} in order to obtain a less noisy image. The objective of this phantom was to test how the process described in figure 3.8 affects the image contrast.

The results of these tests will be presented in section 4.1.3.3.

3.9.2 Real Data

Since the simulated data allows for a better control of the setup conditions, the amount of tests performed with this type of data is greater.

The only test performed with real data was to verify the efficacy of the reconstruction procedure described in figure 3.8.

In order to test the efficacy of the procedure, one needs to have a reference

image. Unlike the previous tests, there is no true sinogram file that could be used to reconstruct a reference image. However, the tracer concentration is approximately uniform, thus, a uniform cylinder image could be used as an emission image for the scatter estimation. The resulting scatter distribution can then be used to correct the prompt data and reconstruct a reference image. The attenuation map was used as both the emission image and attenuation map for the scatter estimation, due to the fact that it is a uniform image with the same geometry as the phantom.

Results and Discussion

The results acquired in this thesis will be described and discussed in this chapter.

The chapter is divided into two main sections: one for the results acquired with simulated data (section 4.1) and one for the results acquired with real data (section 4.2). The former is further subdivided into three subsections, each one related to the results of a specific set of tests:

- Section 4.1.1 will present the results of the tests described in section 3.9.1.1;
- Section 4.1.2 will present the results of the tests described in section 3.9.1.2;
- Section 4.1.3 will present the results of the tests described in section 3.9.1.3. This section is further subdivided into three more subsections, each one concerning the evaluation of one different error source.

Finally, section 4.2 will discuss the results acquired with the use of real data.

4.1 Simulated Data

4.1.1 Comparison of the Scaling Methods

The distribution of the scaling factors calculated by the different methods have shown to have a Gaussian distribution with a mean equal to 1 and a standard deviation (σ_{std}) dependent on the level of statistics of the simulated data (figure 4.1) and on the applied scatter scaling method (figure 4.2). The value of the mean is due to the design of the experiment, in which the scatter distribution that was introduced in the prompt data prior to the introduction of noise is the same that is used for scaling (section 3.7). Therefore, the correct scaling factor is 1.

Figure 4.1 shows the distribution of the acquired scaling factors for the ML method at different statistics. As one can see, the amount of statistics influences the accuracy of the estimation of the scaling factor. The reduction in the number of counts increases the standard deviation of the distribution of the scaling factors.

This is due to the level of the statistical uncertainties, which become greater at lower counts (section 2.3). Therefore, the lower the number of counts, the lower the SNR, thus, the estimation of the scaling factor becomes less accurate.

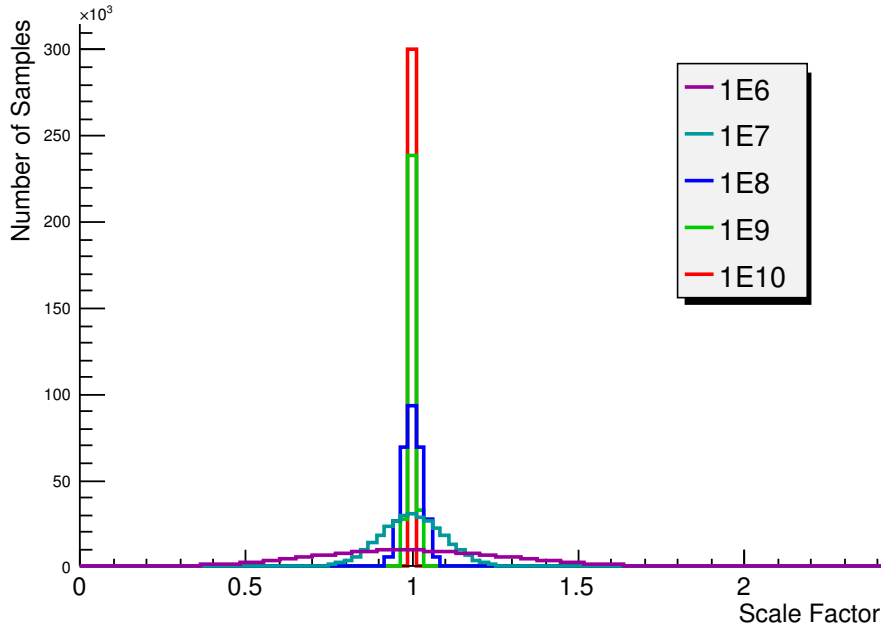


Figure 4.1: Distribution of the scaling factors for the ML method at different levels of statistics.

Another effect that can be seen in figure 4.1 is the apparent “clipping” of the left side of the distribution with the lowest statistics (1×10^6). This is due to the implementation of the ML method, which explicitly rejects the negative scaling factors by setting them to 0. This was not implemented in the other methods, but it is a reasonable procedure, since the value of the scatter cannot be negative due to physical constraints. These cases are rare and only occur at very low statistics. It occurred approximately 16 times in the 300 000 samples of the data set with the lowest statistics. The data sets with higher statistics did not show this behaviour.

When comparing the various scaling methods at the same level of statistics, the standard deviation of the Standard scaling method seems to be the greatest, followed by the NPCD method and the ML method (figure 4.2). The difference between the first two has also been show to be less than the difference between the ML and the NPCD methods for all the samples. This indicates that, for a single plane, the methods proposed perform better than the Standard method.

Figure 4.3 shows the value of the standard deviation for all the methods at different levels of statistics. The ML method provides the lowest standard deviation at all statistical levels, followed by the NPCD method and the Standard method.

The improvement shown in figure 4.3 should be better quantified. Figure 4.4 shows the percentage of the reduction in the standard deviation achieved by the NPCD and the ML methods, relative to the Standard method. The improvement

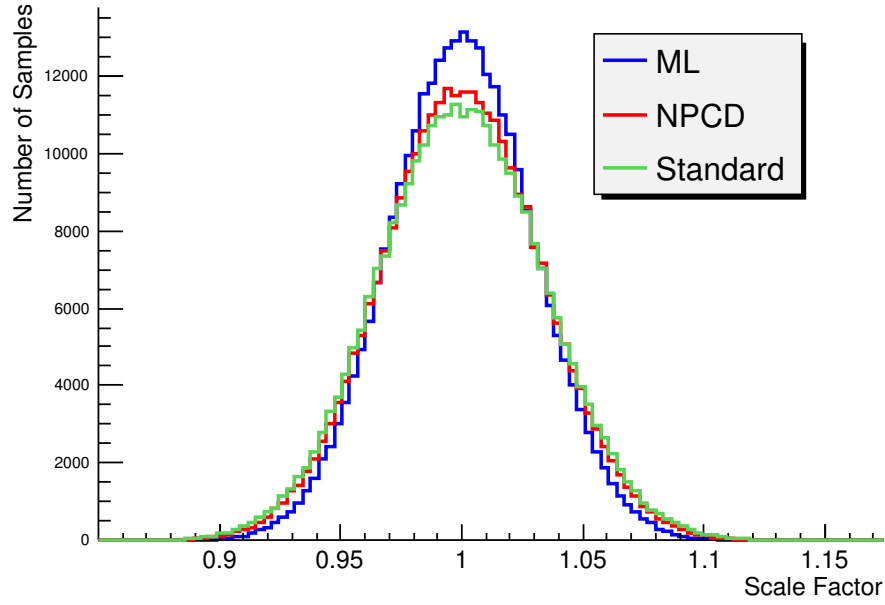


Figure 4.2: Distribution of the scaling factors for all the methods for the data set with 1×10^8 true counts.

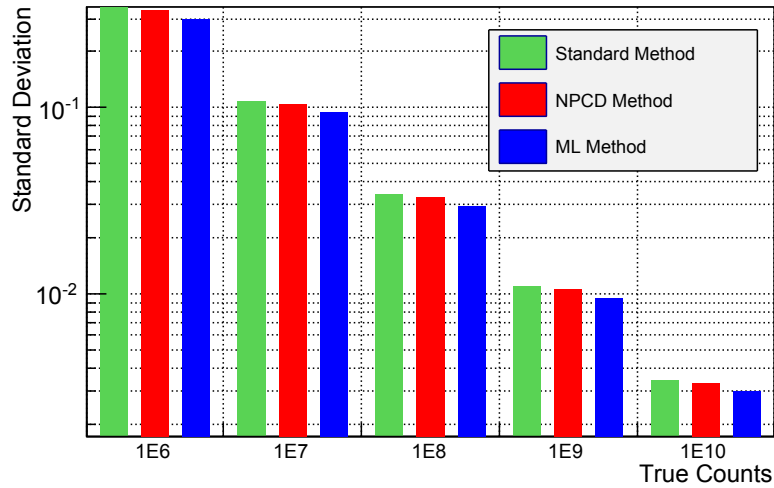


Figure 4.3: Standard deviation values for the three methods at different levels of statistics.

provided by both methods seems to be independent on the level of statistics. The NPCD method provides an improvement around 4% and the ML method slightly above 13%.

The improvement provided by the ML method over the other methods is possibly due to its approach, which takes the Poisson noise characteristics appropriately into account in the estimation of the scaling factor.

Despite the improvement provided by the ML method, it presents at least one disadvantage: it is more time-consuming than the other two methods. Currently, it takes approximately 3 min to scale an entire sinogram file (without PI). However, the time consumed by the ML method is still less than the time consumed by

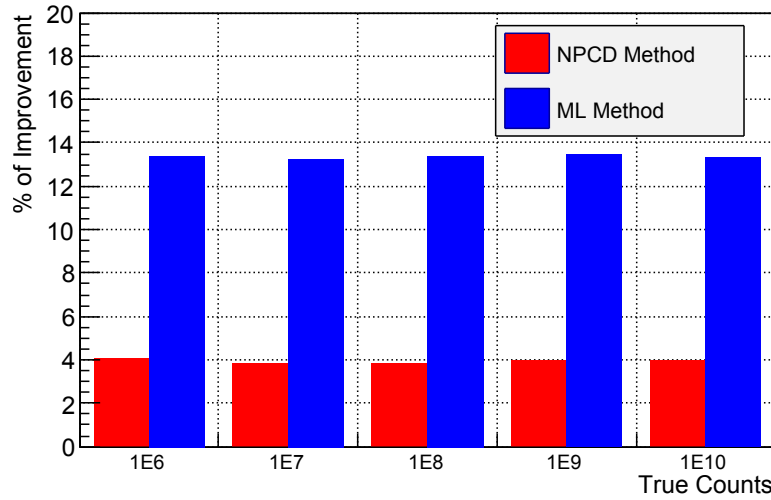


Figure 4.4: Reduction of the standard deviation values relative to the Standard scaling method. All the values are in percentage. Each percentage is calculated as follows: $100 * (\sigma_{\text{std}}(\text{Standard method}) - \sigma_{\text{std}}(\text{method})) / \sigma_{\text{std}}(\text{Standard method})$.

a standard image reconstruction using 32 iterations and 2 subsets (~ 11 min). Therefore, this should not be an impediment to the incorporation of this method in routine procedures. Also, a more efficient implementation of the ML method and the adequate selection of the required precision in the estimation of the maximum $\ln(\mathcal{L}_p)$ value (equation 3.7) should increase the speed of the algorithm.

4.1.2 Plane Integration *versus* Boxcar Filter

Figure 4.5 shows the values of the standard deviation for the NPCD method at different statistics and by using different plane margins for the boxcar filter. As one can see, the standard deviation decreases with the plane margin and with the increase in the number of counts.

Since the results for the Standard method follow the same shape as the ones presented in figure 4.5, these will not be presented.

The ML method also showed a similar distribution (figure 4.6).

The pattern shown in figures 4.5 and 4.6 indicates that both the amount of statistics and the number of planes used for the estimation of the scaling factors have a very strong influence in the value of the standard deviation. In some cases, the standard deviation for a certain level of statistics is even smaller than in a case with better statistics, provided that the former uses more planes to accumulate statistics for the evaluation of the scaling factor. One example of this can be seen in figure 4.5, where the standard deviation value for the 1×10^6 sample with a plane margin of 7 is smaller than the one for the 1×10^7 sample with a plane margin of 0 (single plane).

As stated in section 2.3, the Poisson noise has a greater effect at smaller statistics. Therefore, the higher the statistics, the more accurate should be the estimation of the scatter scaling factor and, consequently, the lower the standard deviation of its distribution. For the same level of statistics, the use of a larger

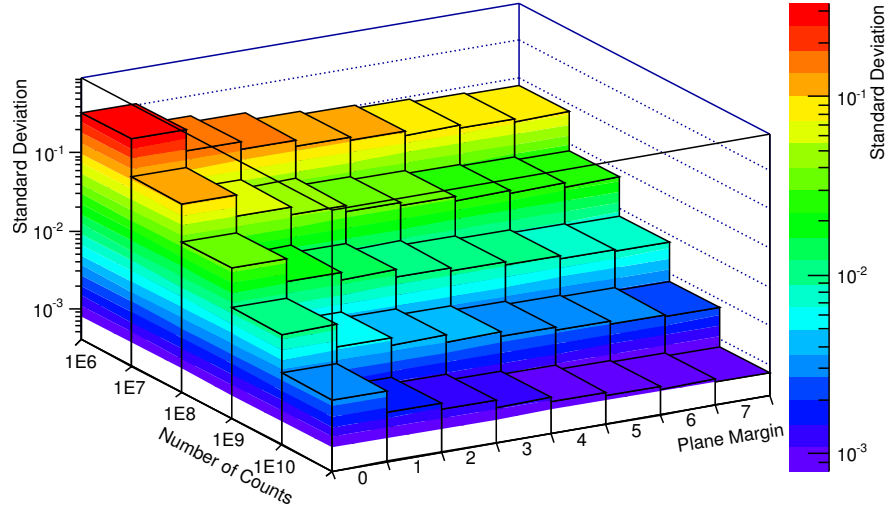


Figure 4.5: Plot of the standard deviation values for different statistics using the NPCD method with a boxcar filter. The plane margin of the boxcar filter varies from 0 (single plane) to 7 (as used by the Siemens software packages).

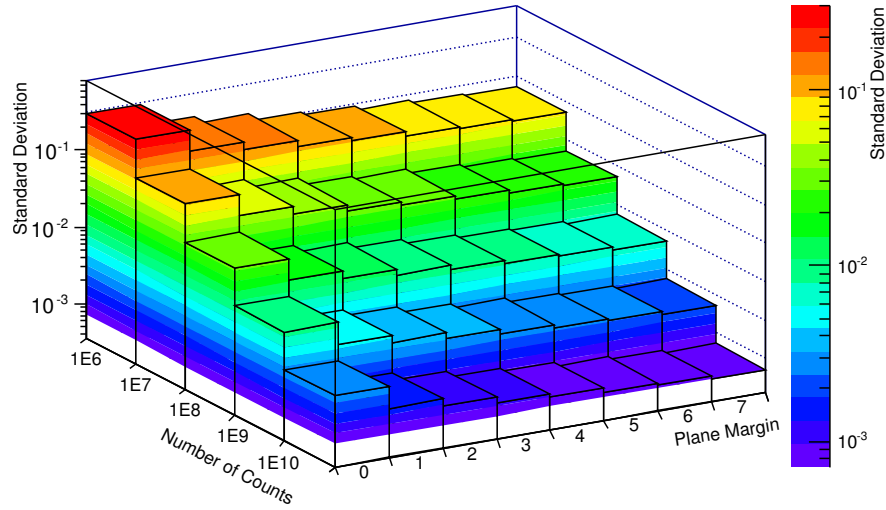


Figure 4.6: Plot of the standard deviation values for different statistics using the ML method with a boxcar filter. The plane margin of the boxcar filter varies from 0 (single plane) to 7 (as used by the Siemens software packages).

plane margin means that more data is used to estimate the scatter scaling factor of a plane p . This is true for both methods, i.e. using directly PI or applying a boxcar filter to the scaling factors, which means that these methods should increase the accuracy of the scatter scaling factor estimations.

Generally, the use of more planes to estimate the scaling factor increases its accuracy. The main objective of this section is to compare between the use of a boxcar filter and PI to see if there is any real advantage of using one over the other.

In the case of the NPCD method there does not seem to be any advantage of using one over the other. As one can see in figure 4.7, the percentage of improvement is very small and it is different for each case. In some cases, the use of PI increased the standard deviation of the distribution of the scaling factors, as one can see by the presence of negative values in the percentages.

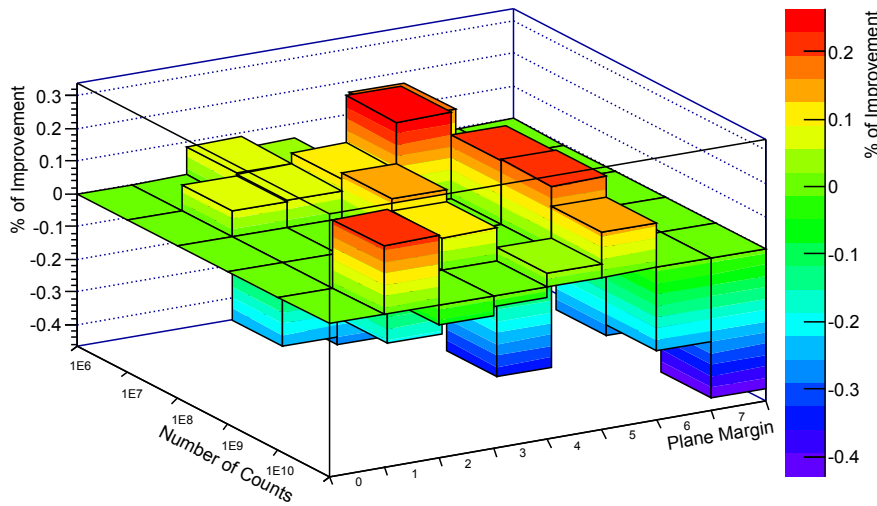


Figure 4.7: Percentage of improvement in each case by using the NPCD method with PI instead of the boxcar filter.

Using PI with the Standard method also did not show any clear advantage or disadvantage of using it over the boxcar filter. The resulting plot shared the same characteristics with the plot in figure 4.7 (small positive and negative percentage values), however, the shape was different.

The ML method seems to behave differently than the other two methods. According to figure 4.8, there seems to be an improvement of approximately 1% at all statistical levels if one chooses to use the PI instead of the boxcar filter. The difference in the results of the ML method might be due to the different approach that this method has compared to the other ones, in which the Poisson noise is directly accounted for.

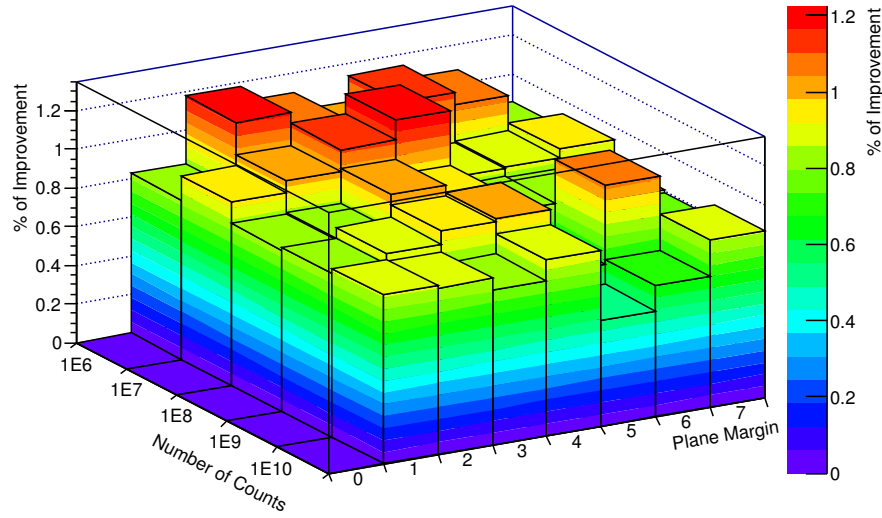


Figure 4.8: Percentage of improvement in each case by using the ML method with PI instead of the boxcar filter.

4.1.3 Evaluation of Error Sources

The following sections will present and discuss the results obtained by introducing errors in the data.

All the sinogram profiles shown are averaged, which means that they are the result of averaging the projection values for all the views in all the planes. This was done to reduce the noise and to obtain a smooth representation.

4.1.3.1 Error in the Scatter Scaling Factor

The correctly scaled scatter sinograms were scaled down by 10% and scaled up by 10%. The averaged scatter tails resulting from these sinograms can be seen in figure 4.9, where 1.0 represents the accurately scaled tails (which almost completely overlap the prompts), 0.9 the underestimated tails and 1.1 the overestimated tails.

Despite the apparent small differences between the tails, these have a considerable influence in the centre of the sinograms, as one can see in figure 4.10.

The reconstructed images for the over/underestimation of the scattering showed a clear bias. However, it is not very clear when seen in an image in grey scale. Therefore, the results regarding images will be presented in intensity profiles. An averaged image profile for each case can be seen in figure 4.11.

The underestimation of the scatter causes an overestimation of the image intensity and the overestimation of the scatter causes an underestimation of the image intensity. The characteristic fluctuations in each profile are common to the three profiles because the statistical simulations used were identical. This means that if each profile is divided by the profile corresponding to 1.0, then, these fluctuations are eliminated.

Figure 4.12 shows the centre of the profiles after being divided by the correctly scaled profile. The ratios between each profile can be seen more clearly.

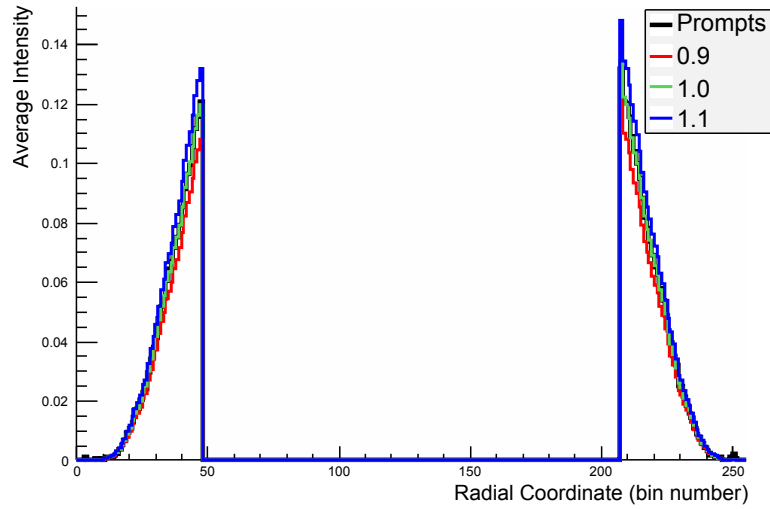


Figure 4.9: Averaged profiles of the simulated scatter tails of a uniform cylinder phantom. 1.0 corresponds to the accurately scaled scatter tails, 0.9 corresponds to the underestimated tails and 1.1 to the overestimated tails.

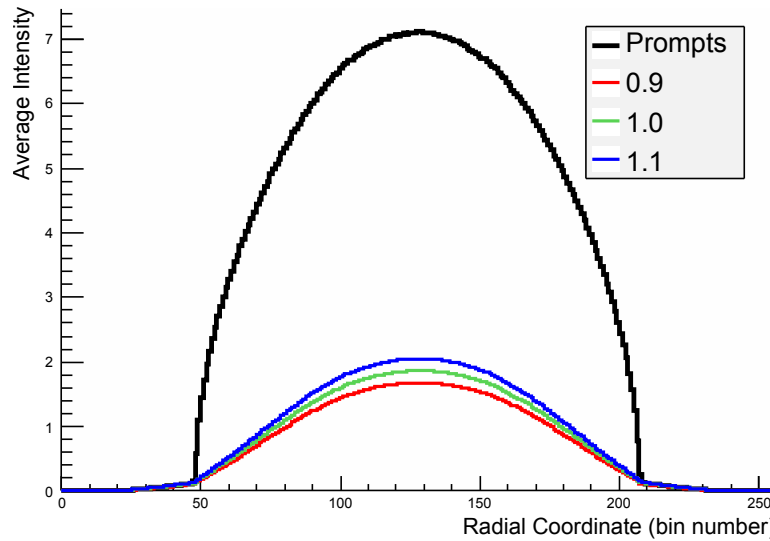


Figure 4.10: Averaged profiles of the simulated scatter sinograms of a uniform cylinder phantom. 1.0 corresponds to the accurately scaled scatter sinograms, 0.9 corresponds to the underestimated sinograms and 1.1 to the overestimated sinograms.

To obtain an approximated value of the bias in each case, a Region Of Interest (ROI) was defined and the average intensity value for each case was calculated. The ROI consisted in a cylinder centred inside the cylinder phantom with a 10 cm diameter and considering the z planes from number 56 to 96. This ROI was also used in the subsequent tests (sections 4.1.3.2, 4.1.3.3 and 4.2).

The mean intensity difference between the 0.9 and 1.0 profiles in the ROI was approximately 4.4%, while the difference between the 1.0 and 1.1 profiles was approximately -4.4%. These values are close to what can be observed in figure 4.12.

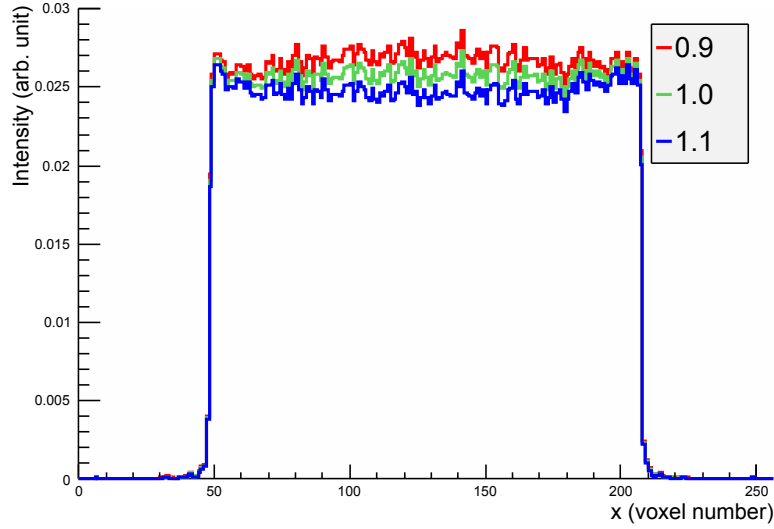


Figure 4.11: Averaged image profiles for the data set with 1×10^8 true counts using different scatter scaling factors. x profile with $y = 128$ and z from 56 to 96. The images were reconstructed using OP-OSEM with 8 iterations and 2 subsets.

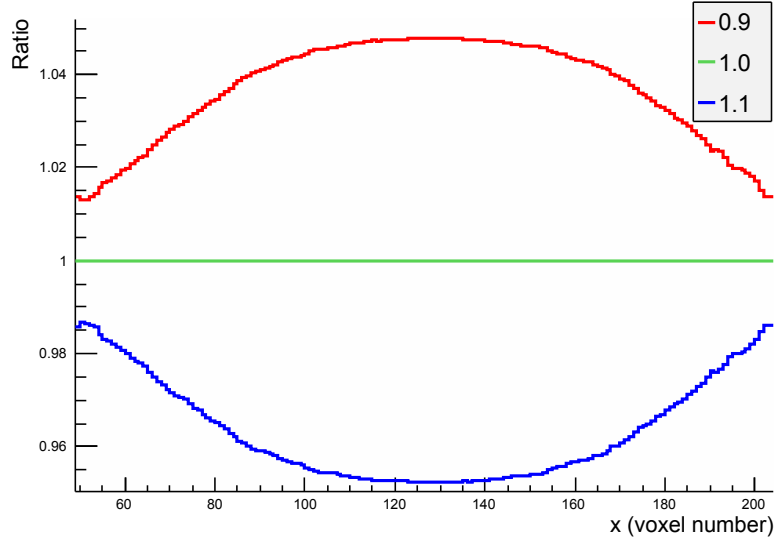


Figure 4.12: Ratio of the centre of the profiles in figure 4.11, relative to $\alpha_p = 1.0$. x profile with $y = 128$ and z from 56 to 96.

The underestimation of the scatter will cause an overestimation of the image intensity because the amount of scatter that will be corrected for is smaller than the amount present in the data. Therefore, some scattered counts will remain in the prompts sinograms, increasing the intensity of the image. This effect is more pronounced in the centre (figure 4.12) because it is the region in this object with a greatest amount of scattered counts (figure 4.10). An analogous argumentation holds in the case of an overestimation of the scatter.

The incorrect estimation of the scatter scaling factor by 10% will not always cause a bias of around 4%. This depends on the amount of scatter in the ROI

(figure 4.10) and the overall scatter fraction of the data. The simulated prompts sinograms had 30% of scattered counts, this can be higher in measured data [Fahey, 2002, Gaens, 2010, Lohmann, 2012]. Therefore, if the scatter fraction in the prompt data is higher, a larger bias can be expected in the reconstructed images.

4.1.3.2 Error in the Random Estimation

The effect that the randoms have on the estimation of the scatter scaling factor is shown in figure 4.13. Here, the randoms sinograms were explicitly scaled by 0.9, 1.0 and 1.1. Since the results were similar for all scaling methods, only the results obtained using the ML method are plotted. Here, the incorrect estimation of the random events introduces a bias on the scaling of the scatter tails.

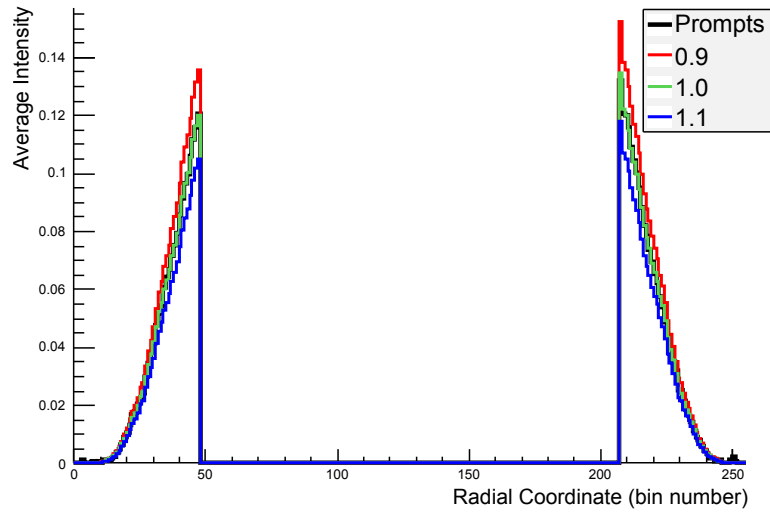


Figure 4.13: Averaged profiles of the simulated scatter tails of a uniform cylinder phantom. 1.0 corresponds to the tails scaled with the use of the correctly scaled randoms sinograms; 0.9 corresponds to the tails scaled with the use of the underestimated randoms sinograms; 1.1 corresponds to the tails scaled with the use of the overestimated randoms sinograms. The scaling was performed with the ML method.

The induced difference between the tails causes pronounced deviations in the centre of the scatter sinograms (figure 4.14). The observed differences have a similar magnitude with respect to the previous case (figure 4.10).

The underestimation of the randoms causes an overestimation of the scatter scaling factor, which in turn will cause an underestimation of the image intensity. The overestimation of the randoms causes the opposite effect.

This can be explained with equation 3.1. The random counts are subtracted from the prompts in the nominator of the division. Thus, the smaller the number of random counts, the greater will be the nominator and, consequently, the estimated scaling factor. The equations of the other methods have an equivalent behaviour. Consequently, a reduction in the random counts causes an increase in the scaling factor, and *vice versa*.

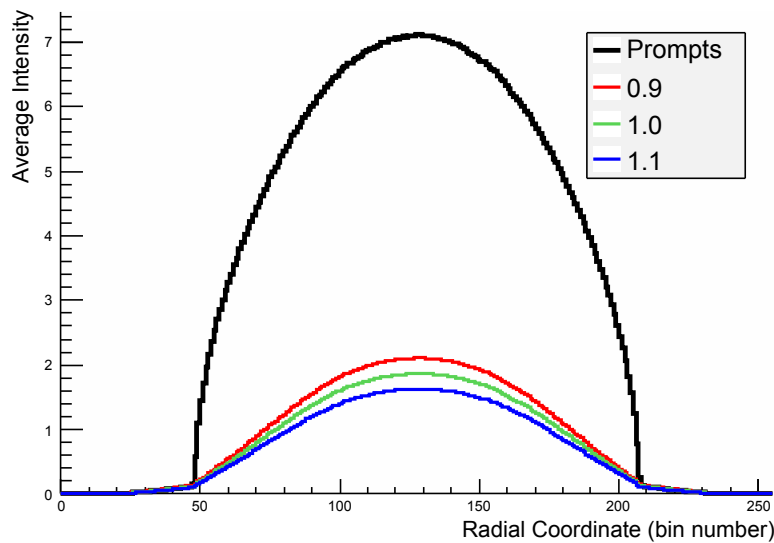


Figure 4.14: Averaged profiles of the simulated scatter sinograms of a uniform cylinder phantom. 1.0 corresponds to the tails scaled with the use of the correctly scaled randoms sinograms; 0.9 corresponds to the tails scaled with the use of the underestimated randoms sinograms; 1.1 corresponds to the tails scaled with the use of the overestimated randoms sinograms. The scaling was performed with the ML method.

The effects of the change in the scaling of the randoms can be clearly seen in the image profiles (figure 4.15). Unlike in the previous test (section 4.1.3.1), the underestimation of the randoms causes an underestimation of the image intensity and the overestimation of the randoms causes an overestimation of the image intensity.

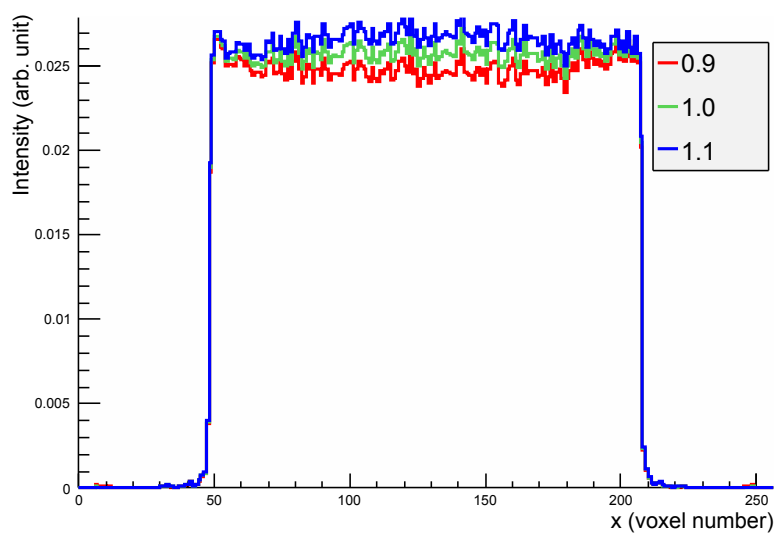


Figure 4.15: Averaged image profiles for the data set with 1×10^8 true counts using different scaling of the randoms sinograms. x profile with $y = 128$ and z from 56 to 96. The images were reconstructed using OP-OSEM with 8 iterations and 2 subsets.

Analogously to section 4.1.3.1, the ratios between the profiles are obtained by dividing modified profiles (0.9 and 1.1) by the nominal profile (1.0). The results are shown in figure 4.16.

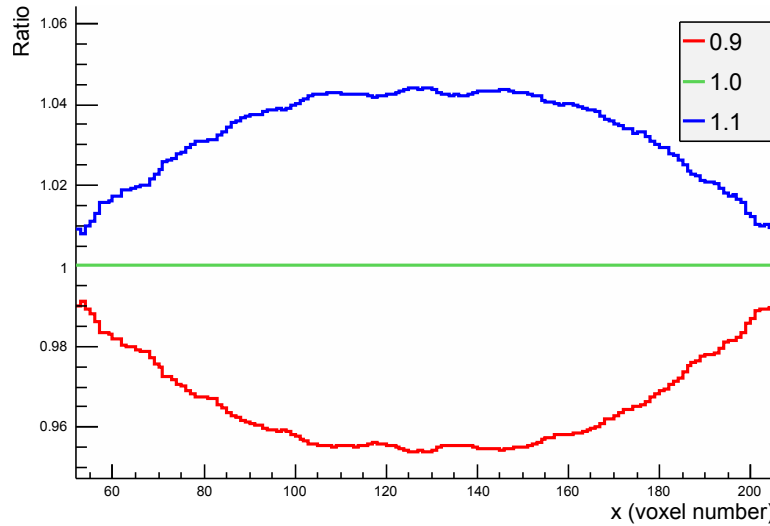


Figure 4.16: Ratio of the centre of the profiles in figure 4.15, relative to the correctly scaled randoms sinograms (1.0). x profile with $y = 128$ and z from 56 to 96.

Despite the slight difference between the shapes of the curves shown in figures 4.12 and 4.16, the bias has nearly the same magnitude. Moreover, when the average intensities in the ROI¹ were calculated, the difference between the 0.9 profile and 1.0 profile was approximately -4.2% and the difference between the 1.1 profile and 1.0 profile was approximately 4.1%. These values are comparable to those in section 4.1.3.1.

The bias in the image profiles are explained by the bias in the scatter scaling factor estimation (section 4.1.3.1). However, the shapes of the curves in figure 4.16 are different from the ones in figure 4.12 due to the fact that there is another factor influencing the reconstruction of these images: the randoms correction. While the introduction of the incorrect randoms sinograms in the estimation of the scaling factor causes a bias, it will also affect the randoms correction of the image. Thus, the randoms correction will not be performed accurately, which originates the small fluctuations seen in the ratios of the image profiles (figure 4.16).

The incorrect estimation of the random counts by 10% will not always cause a bias of around 4% in the ROI. The simulated randoms sinograms have been set to 20% of prompt counts. This setup can significantly differ for real data. For example, the data acquired for this thesis (section 3.8) had a random fraction slightly above 50%. If the data have a random fraction higher than 20%, then, a 10% deviation in the random counts will cause a greater bias in the estimation of the scatter scaling factor. Moreover, if the scatter fraction is higher, the deviation in the scaling factor will increase the bias in the reconstructed image even more (as explained in section 4.1.3.1).

¹see section 4.1.3.1 for details

4.1.3.3 Use of the Reconstructed Image to Estimate the Scatter Distribution

In the previous sections, the emission image used by the SSS to estimate the scatter sinograms was the phantom image from which the true sinograms were generated. Thus, the used scatter sinograms were unbiased and had no noise.

However, in a PET measurement the true distribution is not directly known. In a first approximation, the only image that can be used to estimate the scatter sinograms is the image that has been normalised and corrected for attenuation and random counts: the RA image (figure 3.8).

Two reconstructions of the scatter corrected image (RAS image) were performed: one using the phantom image to estimate the scatter distribution and another using the RA image for the same task. The results show a bias in the RAS image intensity when using the RA image to estimate the scatter distribution (figure 4.17).

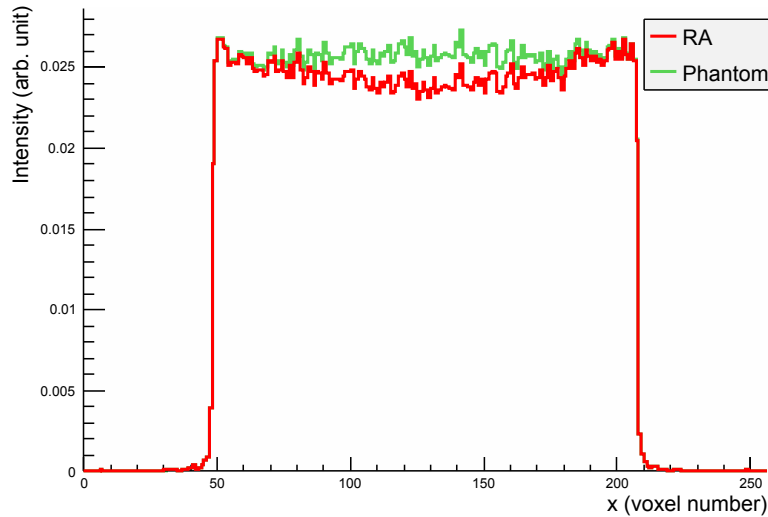


Figure 4.17: Averaged image profiles for the data set with 1×10^8 true counts using the scatter sinograms estimated from the RA image and from the phantom image. x profile with $y = 128$ and z from 56 to 96. The scatter scaling was performed using the ML method and the images were reconstructed using OP-OSEM with 8 iterations and 2 subsets.

It is possible to correct for this effect in simulated data if the scatter estimation and consequent reconstruction of the corrected image are performed more than once.

After the RA image is reconstructed and used to estimate the scatter, this is corrected for scatter and reconstructed. The final image after this first step shall be referred to as RAS_00 and, as one can see in figure 4.18, it is biased. This image is then used to estimate the scatter distribution and the process is repeated several times. The resulting images will become closer to the image obtained by reconstructing the sinograms containing only the true counts (figure 4.18).

The number of iterations needed to recover the true distribution depends on

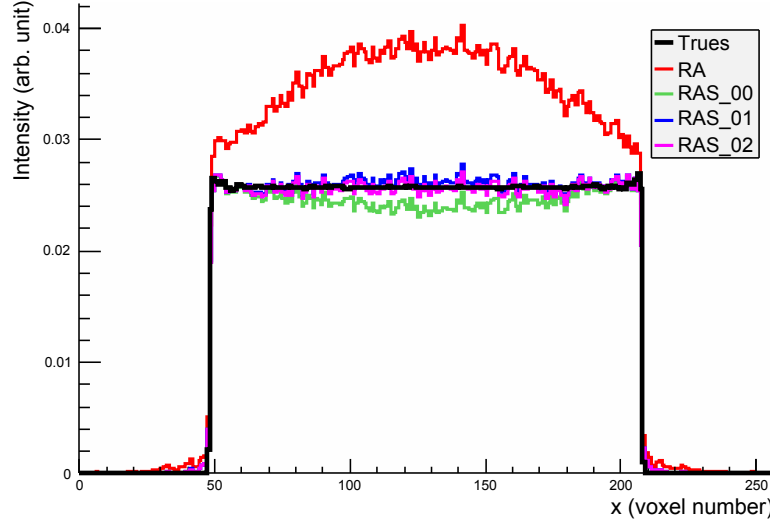


Figure 4.18: Averaged image profiles for the data set with 1×10^8 true counts using the reconstructed images to estimate the scatter distribution (30% scatter fraction). The profiles show the several iterations that took for the RAS profile to converge to the profile acquired reconstructing the sinograms with only the true counts. x profile with $y = 128$ and z from 56 to 96. The scatter scaling was performed using the ML method and the images were reconstructed using OP-OSEM with 8 iterations and 2 subsets.

the scatter fraction. If the scatter fraction in the data is increased from 30% to 50%, the convergence will be slower (figure 4.19).

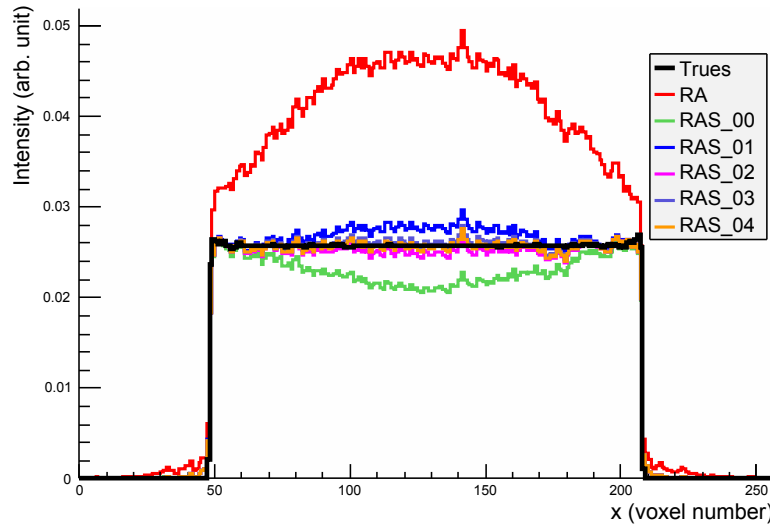


Figure 4.19: Averaged image profiles for the data set with 1×10^8 true counts using the reconstructed images to estimate the scatter distribution (50% scatter fraction). The profiles show the several iterations that took for the RAS profile to converge to the profile acquired reconstructing the sinograms with only the true counts. x profile with $y = 128$ and z from 56 to 96. The scatter scaling was performed using the ML method and the images were reconstructed using OP-OSEM with 8 iterations and 2 subsets.

Figure 4.20 shows the difference in the ROI² as a function of the number of iterations for the two values of scatter fraction. After the process of estimating the scatter distribution with the RAS image has been repeated 10 times, the final deviation in the intensity is below 0.3% (approximately) for both 30% and 50% scatter fractions.

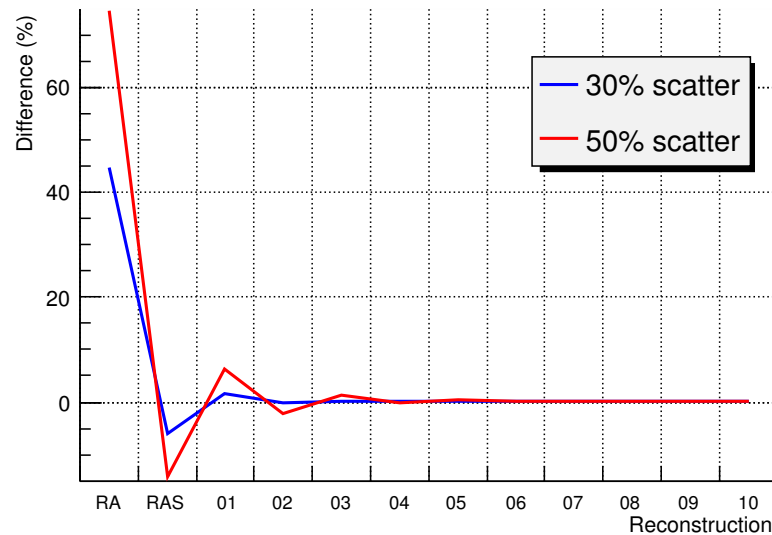


Figure 4.20: Intensity differences in the ROI with the number of iterations used and for different scatter fractions (simulated data).

A more complex phantom was generated by setting the central region intensity to half of the rest of the cylinder while keeping the attenuation map the same (section 4.1.3.3). This was done to see if the intensity ratio could be recovered by using the same method as for the uniform phantom. The OP-OSEM reconstructions used more iterations and subsets than the ones before because in this case it is necessary to obtain sharper images.

Figure 4.21 shows that by reconstructing the image using the phantom to estimate the scatter distribution (RAS_T0), the profile approximates the one obtained by reconstructing the image using the sinograms containing only the true counts (Trues). It also shows that after several iterations, the image will approximate to the phantom image.

²see section 4.1.3.1 for details

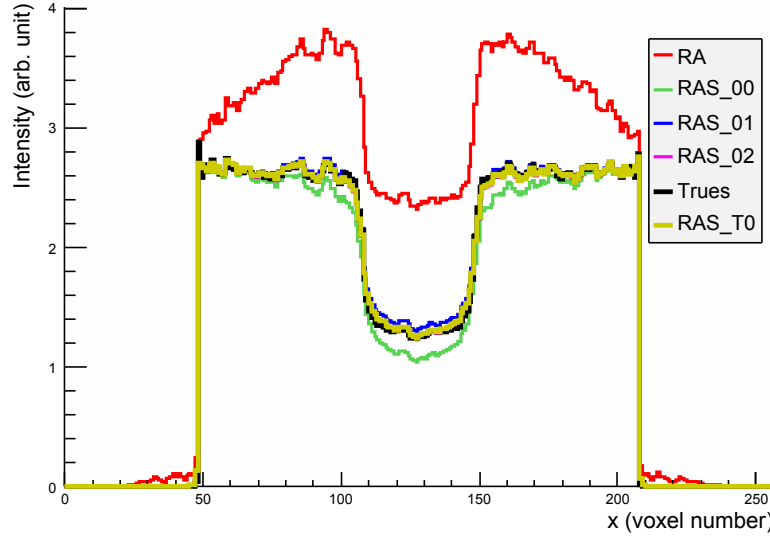


Figure 4.21: Averaged image profiles for the data set with 1×10^{10} true counts using the reconstructed images to estimate the scatter distribution (30% scatter fraction). The profiles show the several iterations that took for the RAS profile to converge to the profile acquired reconstructing the sinograms with only the true counts. x profile with $y = 128$ and z from 56 to 96. The scatter scaling was performed using the ML method and the images were reconstructed using OP-OSEM with 15 iterations and 4 subsets.

4.2 Real Data

Since in real data there is no phantom image from which to estimate the scatter distribution, the RA image was used for this task. The obtained results showed a bias, so the method used in section 4.1.3.3 was applied.

In this case, the scaling method implemented in the Siemens software packages was used to make sure that the standard procedure was followed.

Although there is no phantom image available for the emission distribution, the tracer concentration is approximately uniform. Thus, a uniform cylinder can be used as an emission image for the scatter estimation. The attenuation map was used as both the emission image and attenuation map for the scatter simulation in order to reconstruct a reference image (RAS_T0).

Figure 4.22 shows that the reference image profile is biased (RAS_T0), since it should be uniform. Also, even after several iterations, the image profile will neither approximate the reference profile or an unbiased result (since the RAS_04 profile is still biased).

Figure 4.23 shows the intensity difference in the ROI³ between the RAS_T0 image and the images reconstructed using the process represented in figure 3.8. After the fourth repetition (shown in figure 4.22), the image profile does not change much more (figure 4.23). This means that it will not converge to the RAS_T0 profile or to an unbiased profile. The final intensity profile will be overestimated when compared to an unbiased flat profile.

³see section 4.1.3.1 for details

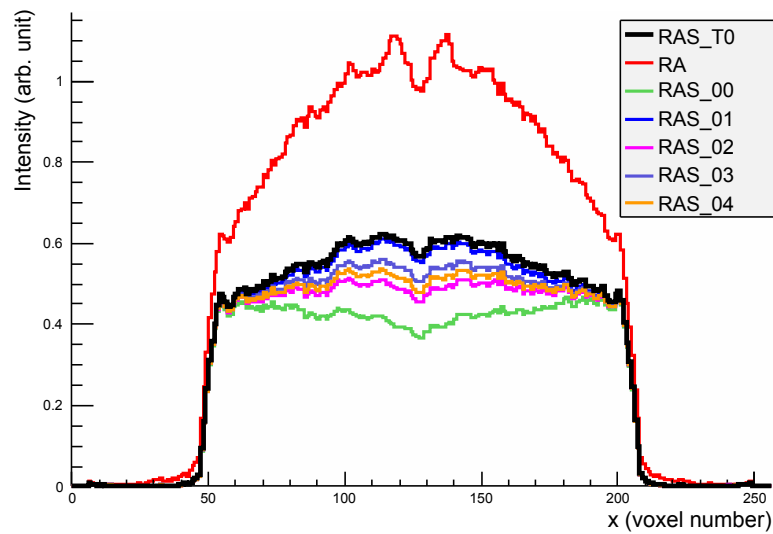


Figure 4.22: Profiles of the images reconstructed with real data.

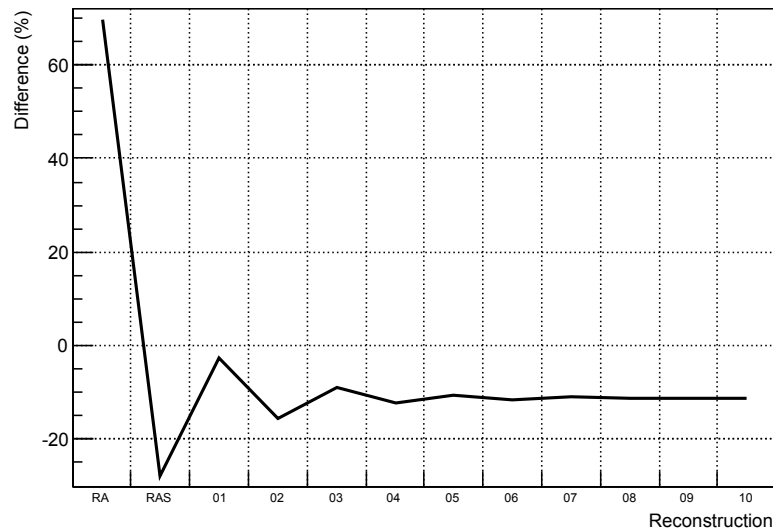


Figure 4.23: Intensity differences in the ROI with the number of iterations used (real data).

The intensity overestimation in these images indicates that the SSS algorithm is underestimating the scatter. One possible explanation for this is that the multiple scatter fraction in the real data provides a broader distribution for the scattering compared to the SSS.

The SSS algorithm is not designed to take multiple scattering correctly into account (section 2.6.4.2). Therefore, the amount of scatter in the image might be underestimated. The results with simulated data showed that several reconstructions and scatter estimations were needed to finally reconstruct an unbiased image. Here, for the simulated data the consistency of the scatter distribution is guaranteed, since the SSS has been taken to generate the underlying scatter background with matching corrections for the reconstruction.

Conclusion

Like any medical imaging modality using high energy photons, PET suffers from several problems, being Compton scattering one of the most important. This phenomenon deflects the annihilation γ photons from their original paths, leading to the incorrect definition of the LORs and consequent degradation of image contrast.

Several strategies have been developed to solve this problem. One of the proposed approaches is to use physical models to estimate the scatter distribution. Among these, the SSS algorithm is one of the most used.

The SSS provides a good scatter estimation within a reasonable computational time. However, the provided scatter distributions are not quantitative. Thus, the obtained scatter estimation has to be scaled appropriately using the scatter tails as reference. This might represent a problem since the tails have very low counts, which makes them very susceptible to Poisson noise.

Two alternative scatter scaling methods were proposed and compared with the method currently used for scatter correction of the BrainPET scanner at the Forschungszentrum Jülich. The results show that both methods perform better than the Standard method. The NPCD method and the ML method show an improvement of the standard deviation of 4% and 13%, respectively. The the ML method can even provide an additional 1% of improvement if the plane integration method is used instead of the currently used boxcar filter.

All three scaling methods behave in the same way in the presence of errors in the data. The influence of each error source has been studied to see their influence in the final image. The results should be useful as a future reference when trying to identify an error source in the data.

Another issue of the SSS is addressed by the required emission image which is usually not known before reconstruction. Unbiased results can only be expected when using the true emission image for the SSS. This issue can be solved for simulated data if the scatter estimation and image reconstruction are repeated several times with successive improvement of the emission images. This has been verified even for high scatter fractions or more complex objects. Usually, unbiased

results can be obtained due to the fact that the simulated scatter distribution is consistently corrected after several iterations.

In contrast to using simulated data with consistent scatter distribution and corresponding corrections, real data revealed some limitations of the SSS approach. For example, data acquired with a homogeneously filled cylinder phantom was reconstructed. However, for real data, after applying the repetitive step of the scatter estimation and subsequent reconstruction, a remaining bias is observed. The SSS cannot fully describe the real scatter distribution since multiple scattering is neglected in this approach. Thus, real scattering data is expected to have broader distributions compared to the estimated by the SSS.

Nevertheless, the results shown in sections 4.1.1 and 4.1.2 suggest that using the ML method with plane integration increases the accuracy of the scatter scaling compared to the standard method, since the ML method is less sensitive to statistical uncertainties. However, this method cannot immediately replace the one implemented in the software packages provided by Siemens. This is due to the fact that these packages are currently used at the Forschungszentrum Jülich for reconstructing patient images. The ML method still needs to be subjected to further tests before it can be used clinically. These tests should include simulated data generated using other approaches and real data.

Currently, there is a toolkit developed at the Forschungszentrum Jülich called PET REconstruction Software TOolkit (PRESTO) [Scheins and Herzog, 2008]. Here, the ML method could be implemented in future versions of PRESTO, thus providing a better scatter scaling to further improve image quality.

References

- Hamamatsu Learning Center: Avalanche Photodiodes. URL <http://learn.hamamatsu.com/articles/avalanche.html>.
- CODATA Value: electron mass:. URL <http://physics.nist.gov/cgi-bin/cuu/Value?me>.
- Roberto Accorsi, Lars-Eric Adam, Matthew E. Werner, and Joel S. Karp. Optimization of a fully 3D single scatter simulation algorithm for 3D PET. *Phys. Med. Biol.*, 49:2577–2598, 2004.
- Lars-Eric Adam, Joel S. Karp, and Richard Freifelder. Energy-Based Scatter Correction for 3-D PET Scanners Using NaI(Tl) Detectors. *IEEE Transactions on Medical Imaging*, 19:513–521, 2000.
- Metin Akay, editor. *Wiley Encyclopedia of Biomedical Engineering*. John Wiley & Sons, Inc., 2006.
- B. Bendriem, R. Trébossen, V. Frouin, and A. Syrota. A PET Scatter Correction Using Simultaneous Acquisitions with Low and High Lower Energy Thresholds. *IEEE*, pages 1779–1783, 1994.
- M. Bergström, L. Eriksson, C. Bohm, G. Blomqvist, and J. Litton. Correction for Scattered Radiation in a Ring Detector Positron Camera by Integral Transformation of the Projections. *Journal of Computer Assisted Tomography*, 7: 42–50, 1983.
- Joseph D. Bronzino, editor. *The Biomedical Engineering Handbook*. CRC Press LLC, 2000.
- Rene Brun and Fons Rademakers. ROOT - An Object Oriented Data Analysis Framework. In *Proceedings AIHENP’96 Workshop, Lausanne*, 1996.
- Jerrold T. Bushberg, J. Anthony Seibert, Edwin M. Leidholdt, and John M. Boone. *The Essential Physics of Medical Imaging*. Lippincott Williams & Wilkins, 2002.
- Simon R. Cherry, James A. Sorenson, and Michael E. Phelps. *Physics in Nuclear Medicine*. Saunders, 2003.

- André Filipe dos Santos Ribeiro. Bone recognition in UTE MR images by artificial neural networks for attenuation correction of brain imaging in MR/PET scanners. Master's thesis, Universidade de Lisboa, 2012.
- Frederic H. Fahey. Data Acquisition in PET Imaging. *Journal of Nuclear Medicine Technology*, 30:39–49, 2002.
- N.C. Ferreira, R. Trébossen, C. Lartizien, V. Brulon, P. Merceron, and B. Bendriem. A hybrid scatter correction for 3D PET based on an estimation of the distribution of unscattered coincidences: implementation on the ECAT EXACT HR+. *Phys. Med. Biol.*, 47:1555–1571, 2002.
- Michaela Gaens. Analysis, Characterisation and Setup of a Block Detector Used in a 3TMR-BrainPET System. Master's thesis, Technische Universität Dortmund, 2010.
- S. Grootenck, T.J. Spinks, D. Sashin, N.M. Spyrou, and T. Jones. Correction for scatter in 3D brain PET using a dual energy window method. *Phys. Med. Biol.*, 41:2757–2774, 1996.
- Technical Information SD-28: Characteristics and use of Si APD (Avalanche Photodiode)*. Hamamatsu, 2004.
- H. Malcom Hudson and Richard S. Larkin. Accelerated Image Reconstruction Using Ordered Subsets of Projection Data. *IEEE Transactions on Medical Imaging*, 13:601–609, 1994. ISSN 0278-0062.
- M. Jacobson, R. Levkovitz, A. Ben-Tal, K. Thielemans, T. Spinks, D. Belluzzo, E. Pagani, V. Bettinardi, M.C. Gilardi, A. Zverovich, and G. Mitra. Enhanced 3D PET OSEM reconstruction using inter-update Metz filtering. *Phys. Med. Biol.*, 45:2417–2439, 2000.
- Philipp Lohmann. Stability and Performance Evaluation of an MR-compatible BrainPET. Master's thesis, FH Aachen, University of Applied Sciences, 2012.
- Mónica Vieira Martins. *3D Image Reconstruction for a Dual Plate Positron Emission Tomograph: Application to Mammography*. PhD thesis, Faculdade de Ciências da Universidade de Lisboa, 2007.
- Nuno Matela. *2D Iterative Image Reconstruction for a Dual Planar Detector for Positron Emission Mammography*. PhD thesis, Universidade de Lisboa, 2008.
- T.R. Oakes, V. Sossi, and T.J. Ruth. Normalization for 3D PET with a low-scatter planar source and measured geometric factors. *Phys. Med. Biol.*, 43:961–972, 1998.
- John M. Ollinger. Model-based scatter correction for fully 3D PET. *Phys. Med. Biol.*, 41:153–176, 1996.

- Irene Polycarpou, Kris Thielemans, Ravindra Manjeshwar, Pablo Aguiar, Paul K. Marsden, and Charalampos Tsoumpas. Comparative evaluation of the scatter correction in 3D PET using different scatter-level approximations. *Ann Nucl Med*, 2011.
- Lucretiu M. Popescu, Robert M. Lewitt, Samuel Matej, and Joel Karp. PET energy-based scatter estimation and image reconstruction with energy-dependent corrections. *Phys. Med. Biol.*, 51:2919–2937, 2006.
- Elena Rota Kops and Hans Herzog. Alternative methods for attenuation correction for PET images in MR-PET scanners. *2007 IEEE Nuclear Science Symposium Conference Record*, pages 4327–4330, 2007.
- Gopal B. Saha. *Basics of PET Imaging: Physics, Chemistry, and Regulations*. Springer, 2005.
- Mitsuhiro Sato, Takayuki Yanagida, Akira Yoshikawa, Yousuke Yatsu, Jun Kataoka, Yoshitaka Ishikawa, and Fumio Saito. Reverse-Type Avalanche Photodiode for Scintillation Detection and Intrinsic Energy Resolution of BGO and GSO:Ce. In *IEEE Nuclear Science Symposium Conference Record*, 2007.
- J. J. Scheins, H. Herzog, and N. J. Shah. Fully-3D PET Image Reconstruction Using Scanner-Independent, Adaptive Projection Data and Highly Rotation-Symmetric Voxel Assemblies. *IEEE Transactions on Medical Imaging*, 30: 879–892, 2011.
- Juergen J. Scheins and Hans Herzog. PET REconstruction Software TOolkit - PRESTO: A Novel, Universal C++ Library for Fast, Iterative, Fully 3D PET Image Reconstruction using Highly Compressed, Memory-Resident System Matrices. In *Nuclear Science Symposium Conference Record*, 2008.
- Heinz-Peter W. Schlemmer, Bernd J. Pichler, Matthias Schmand, Ziad Burbar, Christian Michel, Ralf Ladebeck, Kirstin Jattke, David Townsend, Claude Nahmias, Pradeep K. Jacob, Wolf-Dieter Heiss, and Claus D. Claussen. Simultaneous MR/PET Imaging of the Human Brain: Feasibility Study. *Radiology*, 248:1028–1035, 2008.
- Kengo Shibuya, E. Yoshida, F. Nishikido, T. Suzuki, T. Tsuda, N. Inadama, T. Yamaya, and H. Murayama. Limit of Spatial Resolution in FDG-PET due to Annihilation Photon Non-Collinearity. In *World Congress on Medical Physics and Biomedical Engineering 2006*, volume 14 of *IFMBE Proceedings*, pages 1667–1671. Springer Berlin Heidelberg, 2007.
- Paul Suetens. *Fundamentals of Medical Imaging*. Cambridge University Press, 2009.
- The ROOT Team. *ROOT: Users Guide 5.26*, 2009.

- K. Thielemans, D. Sauge, C. Labbé, C. Morel, M. Jacobson, A. Zverovich, T. Beisel, and Ch. Tsoumpas. *STIR User's Guide Version 2.1*.
- K. Thielemans, R.M. Manjeshwar, Ch. Tsoumpas, and F.P. Jansen. A New Algorithm for Scaling of PET Scatter Estimates Using all Coincidence Events. *IEEE Nuclear Science Symposium Conference Record*, pages 3586–3590, 2007.
- C. Tsoumpas, P. Aguiar, K.S. Nikita, D. Ros, and K. Thielemans. Evaluation of the Single Scatter Simulation Algorithm Implemented in the *STIR* Library. *IEEE*, pages 3361–3365, 2004.
- James E. Turner. *Atoms, Radiation, and Radiation Protection*. Wiley-VCH, 2007.
- Peter E Valk, Dale L Bailey, David W Townsend, and Michael N Maisey. *Positron Emission Tomography: Basic Science and Clinical Practice*. Springer, 2003.
- Floris H. P. van Velden, Reina W. Kloet, Bart N. M. van Berckel, Adriaan A. Lammertsma, and Ronald Boellaard. Accuracy of 3-Dimensional Reconstruction Algorithms for the High-Resolution Research Tomograph. *Journal of Nuclear Medicine*, 50(1):72–80, 2009.
- C.C. Watson. New, Faster, Image-Based Scatter Correction for 3D PET. *IEEE*, pages 1637–1641, 2000.
- Alexander Werling, Olaf Bubltz, Josef Doll, Lars-Eric Adam, and Gunnar Brix. Fast implementation of the single scatter simulation algorithm and its use in iterative image reconstruction of PET data. *Phys. Med. Biol.*, 47:2947–2960, 2002.
- Miles N. Wernick and John N. Aarsvold, editors. *Emission Tomography: The fundamentals of PET and SPECT*. Elsevier Academic Press, 2004.
- H. Zaidi and K.F. Koral. *Quantitative Analysis in Nuclear Medicine Imaging*. Springer, 2006.
- Habib Zaidi and Kenneth F. Koral. Scatter modelling and compensation in emission tomography. *European Journal of Nuclear Medicine and Molecular Imaging*, 31:761–782, 2004.
- Habib Zaidi and Marie-Luise Montandon. Scatter Compensation Techniques in PET. *PET Clin*, 2:219–234, 2007.

Index

- δ ray, 4
- γ photon, 7
- 2D-PET, 12
- 3D-PET, 36

- ACF, 19, 31
- activity, 3, 4
- annihilation, 5, 7
 - photon, 5
- APD, 9, 11, 29
- attenuation, 17
 - coefficient, 17
 - map, 19, 31, 37
 - sinogram, 37
- Auger electron, 6
- avalanche effect, 11

- back-scatter, 6
- backprojection, 24
- Becquerel [Bq], 4
- blank scan, 19
- boxcar filter, 33, 34, 38, 39
- BrainPET, 19, 29, 30, 38
- Bremstrahlung, 5

- changed particles, 4
- Compton scattering, 5, 6, 9
- cost function, 27
- CT, 19

- decay
 - constant, 4
 - factor, 4
- detector block, 9
- DEW, 20
- dynode, 10, 11

- electromagnetic radiation, 4
- electron, 7
- electron cascade, 6
- ETM, 20
- excitation, 5

- FBP, 25
- filtered backprojection, 25, 26
- forward projection, 26, 27
- FOV, 29
- FT, 25
 - inverse FT, 25

- half-life ($T_{1/2}$), 4

- image space, 24, 25
- ionization, 4, 11

- k-space, 25

- LOR, 7, 9, 19
- LSO, 10, 29

- Michelogram, 14
- MLEM, 27
- MR, 11
- multiple coincidence, 8
- multiple scattered event, 23

- neutrino, 3
- neutron, 3
- normalisation, 16
 - component-based normalisation, 16
 - direct normalisation, 16
 - sinogram, 31, 37

- OP-OSEM, 17, 18, 20, 23
- OSEM, 28

- PET, 1
- PET/CT, 19
- PET/MR, 9, 11
- phantom image, 55
- photoelectric effect, 5
- photoelectron, 5, 10
- PI, 36, 38, 39
- PMT, 9
- Poisson
 - distribution, 7
 - noise, 7, 35
- positron, 3, 4, 7
 - decay, 3
 - emission, 3
- PRESTO, 62
- projection slice theorem, 25
- prompt
 - event, 7
 - sinogram, 37
- proton, 3
- RA image, 40, 55
- radionuclide, 3
- radiopharmaceutical, *see* tracer
- ramp filter, 25
- random
 - count, 8
 - event, 7, 17
- randoms
 - sinogram, 17
- RAS image, 40, 55
- ROI, 50
- scaling method
 - ML method, 35
 - NPCD method, 34
 - Standard method, 33
- scatter
 - angle, 6
 - event, 9, 26
 - sinogram, 37
 - tails, 20, 23, 31
- scattered
 - event, 7
- scintillation
 - crystal, 9, 11, 15
 - photon, 10, 11
- secondary
 - electron, 4
 - ionization, 4
- segment, 13
- single scattered event, 9, 23
- sinogram, 12
 - bin, 12, 30
 - file, 30, 38
 - plane, 30, 33
- SNR, 7
- span, 14
- SSS, 6, 20, 21, 23, 31, 55
- tail mask, 33
- TBA, 19
- timing
 - window, 7
- timing window, 17, 30
- tracer, 1, 3, 19
- transmission scan, 19
- true
 - event, 7
- update function, 27
- valence shell, 5
- X-ray
 - characteristic X-ray, 5